NASA Technical Memorandum 84490

COMPARISON OF ANALYTICAL AND EXPERIMENTAL SUBSONIC STEADY- AND UNSTEADY- PRESSURE DISTRIBUTIONS FOR A HIGH-ASPECT-RATIO SUPERCRITICAL WING MODEL WITH OSCILLATING CONTROL SURFACES

WILLIAM E. MCCAIN

AUGUST 1982

National Aeronautics and Space Administration

Langley Research Center
Hampton, Virginia 23665

COMPARISON OF ANALYTICAL AND EXPERIMENTAL SUBSONIC STEADY- AND UNSTEADY-PRESSURE DISTRIBUTIONS FOR A HIGH-ASPECT-RATIO SUPERCRITICAL WING MODEL WITH OSCILLATING CONTROL SURFACES

By William E. McCain

SUMMARY

The results of a comparative study using the unsteady aerodynamic lifting-surface theory, known as the Doublet Lattice method, and experimental subsonic steady- and unsteady-pressure measurements, are presented for a high-aspect-ratio supercritical wing model. Comparisons of pressure distributions due to wing angle of attack and control-surface deflections were made. In general, good correlation existed between experimental and theoretical data over most of the wing planform. The more significant deviations found between experimental and theoretical data were in the vicinity of control surfaces for both static and oscillatory control-surface deflections.

INTRODUCTION

The application of active controls technology, especially in conjunction with such advanced aerodynamic features as winglets and supercritical airfoils, can provide improved aircraft characteristics with relaxed static stability, load alleviation, and flutter suppression systems. The design and analysis of active control systems for energy-efficient transports frequently require multi-purpose computer programs that include unsteady aerodynamic calculations. Programs currently used at Langley Research Center for the synthesis and analysis of active controls include ISAC (ref. 1), SYNPAC (ref. 2), DYLOFLEX

(refs. 3 and 4), and the aerodynamic energy method (ref. 5), all of which use the Doublet Lattice method for unsteady aerodynamics. An active control system design is very sensitive to the quality of the aerodynamic results employed.

To investigate the effects of oscillating control surfaces on unsteady aerodynamics, a series of wind-tunnel tests were conducted by the National Aeronautics and Space Administration (NASA) in the Langley Transonic Dynamics Tunnel (TDT), using a semispan model of a high-aspect-ratio supercritical wing. The primary objective of these tests was to provide a comprehensive data base of measured transonic unsteady pressures for a wing representative of those envisioned for an energy-efficient transport. A secondary objective was to provide similar data at subsonic conditions. The results from these tests are contained in references 6 and 7. These results are in the form of both steady and unsteady pressure distributions for variations in Mach number, Reynolds number, wing angle of attack, control-surface deflection angle (static and oscillating), and control-surface oscillation amplitude and frequency.

The purpose of this paper is to compare the experimental pressure distributions available at Mach number 0.60 with pressure distributions calculated by the Doublet Lattice method. The Doublet Lattice method was chosen because of its extensive use in active controls synthesis and analysis. Exclusive use of Doublet Lattice results in this paper should not be interpreted as disregarding other available methods, such as the Kernel function method of RHOIV (refs. 8 and 9), or the more advanced methods of small-perturbation or full-potential equation formulations (reviewed in refs. 10, 11, and 12). Since it is well known that Doublet Lattice, as well as other lifting-

surface theories, overpredicts control-surface aerodynamics, correction factors are frequently applied to reduce this error (ref. 13). It is hoped that the results of this paper will assist in the development of empirical correction methods that can be applied to the Doublet Lattice calculations.

SYMBOLS

AR	aspect ratio, b_0^2/S
$b_0/2$	wing semispan, m
b	wing root semichord, m
c	streamwise local chord, m
c_{av}	wing average chord, m
c_ℓ	section lift coefficient
c_m	section pitching-moment coefficient about the leading edge
C_p	pressure coefficient
C'_p	lifting-surface steady-pressure coefficient, $C_{p_{l.s.}} - C_{p_{u.s.}}$
$\Delta c_\ell/\Delta\alpha$	increment in section lift coefficient per change in angle of attack, deg^{-1}
$\Delta c_\ell/\Delta\delta$	increment in section lift coefficient per change in control-surface deflection, deg^{-1}
$\Delta c_m/\Delta\alpha$	increment in section pitching-moment coefficient about the leading edge per change in angle of attack, deg^{-1}
$\Delta C'_p/\Delta\alpha$	increment in lifting-surface pressure coefficient per change in angle of attack, deg^{-1}
$\Delta C'_p/\Delta\delta$	increment in lifting-surface pressure coefficient per change in control-surface deflection, deg^{-1}

$\lvert C'_p \rvert$	magnitude of lifting-surface unsteady-pressure coefficient
f	frequency of oscillating control surface, Hz
k	reduced frequency, $b\omega/V$
M	free-stream Mach number
q	free-stream dynamic pressure, kPa
R	Reynolds number based on wing average chord
S	total wing planform area, m^2
t/c	thickness-to-chord ratio
V	free-stream velocity, m/sec
x	streamwise coordinate, m
x/c	fraction of local streamwise chord
y	spanwise coordinate, m
z	vertical coordinate, positive up, m
α	wing angle of attack, deg
δ	control-surface deflection angle, positive trailing edge down, deg
$\Delta\alpha$	change in wing angle of attack, deg
$\Delta\delta$	change in control-surface deflection angle, deg
$\Lambda_{l.e.}$	leading-edge sweepback angle, deg
η	fraction of semispan, $2y/b_0$
ϕ	phase angle of unsteady pressure, referenced to control-surface motion (negative for pressure changes lagging the control-surface motion)
ω	circular frequency of oscillating control surface, rad/sec

Subscripts and Abbreviations

C.S.	control surface
l.e.	leading edge
l.s.	lower surface
ref	reference
u.s.	upper surface

MODELS

Wind-Tunnel Model

A sketch of the wind-tunnel model is presented in figure 1. The model has an aspect ratio of 10.76, a leading edge sweepback angle of 28.8°, and a semispan of 2.286 meters. total of 252 static-pressure orifices were installed on the wing, with half on the upper surface and the other half on the lower surface. The table in figure 1 lists the designated spanwise stations for each of the nine chordwise sets of orifices. A total of 164 dynamic-pressure transducers were installed on the wing at closely-corresponding locations to the static-pressure orifices. The model was equipped with a total of 10 oscillating control surfaces, 5 at the leading edge with hinge lines on the 15 percent chord and 5 at the trailing edge with hinge lines on the 80 percent chord. Only 2 of the 10 control surfaces were considered in this study: an inboard trailing edge control surface and an outboard trailing edge control surface (identified as nos. 6 and 9 in refs. 6 and 7). The inboard control surface is located between 10 and 24 percent semispan, and the outboard control surface is loacted between 59 and 79 percent semispan. The cross-sectional shape of the model consists of

NASA supercritical-airfoil sections of varying chord length and thickness as shown in figure 2. Further details of the wind-tunnel model, including airfoil shape quality and planform rigidity are described in references 6, 7, and 14.

Analytical Model

An aerodynamic model was generated for use in the subsonic unsteady lifting-surface theory known as the Doublet Lattice method (ref. 15). The arrangement of aerodynamic boxes representing the wind-tunnel model is shown in figure 3. To provide more calculated pressure points for comparative purposes, the chordwise and spanwise distribution of aerodynamic boxes were increased over the planform areas near and on the control surfaces. The aerodynamic boxes in figure 3 with asterisks identify the control surfaces and the cross-hatched strips identify the locations corresponding to the nine semispan stations shown in figure 1. There were 42 streamwise strips, a total of 325 aerodynamic boxes, used to comprise the model layout. In creating this box layout, an attempt was made to keep the aspect ratio of each box as close to 1.0 as possible.

EXPERIMENTAL DATA

All the experimental data presented herein were obtained at the test conditions of $M = 0.60$, $R = 2.2 \times 10^6$ (based on the wing average chord), and $q = 3.0$ kPa. The tests included two angles of attack of zero degrees and approximately 2.85 degrees (corresponding to the cruise condition).

Steady-Pressure Data

A summary of the conditions at which the steady-pressure data were taken is presented in Table I. The test point numbers used to identify the data in

reference 7 are listed in the table for convenience. Test conditions for both inboard and outboard control surfaces included seven control-surface deflection angles ranging from -6° to 6°.

The results of reference 14 indicated that the wind-tunnel model was essentially rigid and that pressure-measurement results were not significantly influenced by model flexibility. Therefore, only four rigid body modes (plunge, pitch, inboard, and outboard control-surface deflections) of the model were included in the analysis. Reduced frequencies of 0, 0.14, 0.27, and 0.41 were chosen, corresponding to those at which experimental data were available in reference 7.

The experimental data from ref. 7 consisted of tabulated steady-pressure coefficients, C_p, on both upper and lower surfaces of the wing with the corresponding lifting-surface steady-pressure coefficients, $C'_p = C_{p_{l.s.}} - C_{p_{u.s.}}$. The section lift coefficient, c_ℓ, and section pitching-moment coefficient about the leading edge, c_m, at each of the nine spanwise stations were obtained by numerically integrating equations (1) and (2), respectively.

$$c_\ell = \frac{1}{c} \int_0^1 C'_p \, dx \tag{1}$$

$$c_m = \frac{1}{c^2} \int_0^1 C'_p \, x \, dx \tag{2}$$

Calculations were also made for the incremental changes in these coefficients due to angle of attack or control-surface deflection changes, as follows:

$$\frac{\Delta c_\ell}{\Delta \alpha} = \frac{c_\ell - c_{\ell_{ref}}}{\alpha - \alpha_{ref}} \tag{3}$$

$$\frac{\Delta c_\ell}{\Delta \delta} = \frac{c_\ell - c_{\ell_{ref}}}{\delta - \delta_{ref}} \tag{4}$$

$$\frac{\Delta c_m}{\Delta \alpha} = \frac{c_m - c_{m_{ref}}}{\alpha - \alpha_{ref}} \tag{5}$$

$$\frac{\Delta C'_p}{\Delta \alpha} = \frac{C'_p - C'_{p_{ref}}}{\alpha - \alpha_{ref}} \tag{6}$$

$$\frac{\Delta C'_p}{\Delta \delta} = \frac{C'_p - C'_{p_{ref}}}{\delta - \delta_{ref}} \tag{7}$$

Typically, the referenced quantities corresponded to the zero-valued test conditions.

Unsteady-Pressure Data

A summary of the conditions at which the unsteady-pressure data were taken is presented in Table II. Again, the test point numbers identify the data obtained from ref. 7. Each control surface was oscillated about a zero mean deflection angle with an amplitude of ±4° for three frequencies of oscillation (5, 10, 15 Hz). Depending on the exact tunnel speed for a given test point, the corresponding reduced frequencies varied slightly about the average values of 0.14, 0.27, and 0.41, respectively. The unsteady-pressure measurements are presented in the form of the magnitude of the lifting-surface unsteady-pressure coefficient, $|C'_p|$, and phase angle, ϕ. All phase angles were referenced to the control-surface motion, with negative values for pressure changes lagging the control-surface motion. Although unsteady-pressure measurements were made

at all nine semispan stations, only the chordwise distributions at two locations (one near the center of each control surface--rows 1 and 6 in figure 1) were considered in this study.

ANALYSIS

The Doublet Lattice formulation solves the linearized acceleration or pressure potential-flow equations on zero thickness lifting surfaces at subsonic speeds with nonplanar boundary conditions. The Doublet Lattice method (ref. 15) was used to generate the theoretical steady and unsteady aerodynamics herein. The calculations were performed by the version of the Doublet Lattice program which is used in a NASA computer program system known as ISAC (Interaction of Structures, Aerodynamics, and Controls, ref. 1). As stated previously, four rigid-body modes (plunge, pitch, inboard, and outboard control-surface deflections) were used at four reduced frequencies at a Mach number of 0.60.

For each mode and at each reduced frequency, the output from the Doublet Lattice program consists of complex lifting-surface pressure coefficients on each aerodynamic box. Since the program performs the necessary numerical integrations internally, the complex section lift and moment coefficients are also listed. At zero reduced frequency (steady), the imaginary parts of these complex quantities are zero. The real and imaginary parts of the unsteady quantities were converted to magnitudes and phase angles for direct comparison to the experimental values from ref. 7.

COMPARISON OF ANALYSIS AND EXPERIMENT

Steady-Pressure Results

Comparisons of the incremental lifting-surface pressure distributions for an incremental angle of attack are shown in figures 4(a) to 4(i) at each of the

nine semispan stations. The two sets of experimental data correspond to the zero-deflection-angle data taken for both inboard and outboard control surfaces at an incremental angle of attack. At each semispan station and for approximately the forward 40 percent of the local chord, the Doublet Lattice data noticeably underpredict the magnitude of the chordwise pressure distribution. In addition, for about the aft 40 percent of the local chord, it slightly overpredicts the magnitude. The deviations shown between the experimental and theoretical data are typical of airfoil thickness effects (viscosity), ref. 8.

The next comparison illustrates the integrated result of the local incremental lifting-surface pressure distributions for section lift and pitching-moment coefficients, shown in figures 5(a) and 5(b). Figure 6 presents the spanwise distribution of local aerodynamic center locations. In figures 5 and 6, the two sets of experimental data show good agreement between each other for measurements from approximately 25 to 80 percent semispan. However, there is limited scatter in the experimental data inboard of 25 percent semispan and outboard of 80 percent semispan, possibly due to fuselage-body and tip effects, respectively.

The incremental lifting-surface pressure distributions for incremental control-surface deflections are shown in figures 7 and 8. Figure 7 presents comparisons for the inboard control-surface data at semispan station $\eta = 0.19$; figure 8 presents comparisons for the outboard control surface data at semispan station $\eta = 0.71$. Each figure contains data at the two angles of attack and for three positive and negative incremental control-surface deflection angles ($\Delta\delta = \pm 2°, \pm 4°, \pm 6°$). The magnitudes of the experimental pressure coefficient due to positive (trailing edge down) control-surface deflections are less than

those due to equivalent negative deflections. Although experimental chordwise pressure distributions for either positive or negative control-surface deflections show similar trends, there is better correlation with the theory for the experimental negative deflection data. For both control surfaces, the largest deviation between experimental and theoretical data occurs aft of the hinge line. The more significant difference occurs on the outboard control surface. Note that the experimental data for positive outboard control-surface deflections exhibit a rise in pressure at the 95 percent chord location after dropping to a minimum pressure at the 90 percent chord location. This effect is possibly due to increased spanwise flow or separated flow toward the trailing edge of the deflected control surface. The comparison between experimental and theoretical data forward of each control-surface hinge line shows good correlation in trend, but not in magnitude. The Doublet Lattice data in this region of the chordwise pressure distribution usually underpredicted the inboard measurements and slightly overpredicted most of the outboard measurements. This particular deviation being a percentage difference in magnitudes could be adjusted by correction factors to the Doublet Lattice aerodynamics, similar to those used on control surfaces, ref. 13. There were relatively small differences overall between the respective data sets at each angle of attack.

The incremental section lift coefficient distributions for the incremental control-surface deflections are shown in figure 9. The averaged experimental values shown are for the integrated results of the local incremental lifting-surface pressure distributions due to the six incremental control-surface deflections ($\Delta\delta = \pm 2°, \pm 4°, \pm 6°$). The experimental scatter is indicated by the vertical lines through each symbol. All the experimental incremental section lift coefficients shown are based on the zero angle of attack data. The

experimental averages for the inboard control-surface data show a good comparison with the theoretical results. The experimental averages for the outboard control surface do not compare well with theory. As stated previously, the possible effect of spanwise flow or separated flow in this region could be significant. In addition, from the data presented herein and other data contained in references 6 and 7, there is evidence that small angle of attack or control-surface deflection changes can produce large pressure changes at the outboard semispan stations, η = 0.71, 0.78, 0.81, and 0.92.

Unsteady-Pressure Results

Comparisons of the chordwise unsteady-pressure distributions, in the form of magnitudes and phase angles, are presented in figures 10 and 11. For the three oscillating frequencies of 5, 10, and 15 Hz, the magnitudes and phase angles of the lifting-surface unsteady-pressure coefficients are compared at semispan station η = 0.18 (figures 10(a)-(c)) for the inboard control-surface data, and at semispan station η = 0.71 (figures 11(a)-(c)) for the outboard control-surface data. The experimental data for both angles of attack (zero and cruise) exhibited only minor scatter. Similar to the steady-pressure comparisons, the Doublet Lattice data overpredicted the experimental unsteady-pressure magnitudes aft of the control-surface hinge lines, with the more significant deviation on the outboard control surface. In addition, there is an overprediction of the experimental data at the 75 percent chord of the outboard control surface (immediately forward of the hinge line). The two trailing edge (x/c = 0.90, 0.95) experimental unsteady-pressure measurements also exhibited possible spanwise or separated flow effects on the outboard control surface,

as discussed previously for the steady-pressure data. The experimental and the unsteady-pressure magnitude data show good correlations in trends forward of each control-surface hinge line. Overall the deviation in this region for magnitudes is more significant for the inboard control surface. The Doublet Lattice phase angles were more negative (lagging) than the experimental data toward the leading edge. There was good correlation between theoretical and experimental phase angles in trend. with the best comparison at the in-phase point (ϕ = 0) of approximately 60 percent chord. There is a noticeable deviation between the theoretical and experimental phase angles at the same trailing edge locations of the outboard control surface which have shown possible spanwise or separated flow effects in the pressure magnitude data.

CONCLUDING REMARKS

This paper presents comparisons of theoretical and experimental steady- and unsteady-pressure distributions on a high-aspect-ratio supercritical wing model at M = 0.60. The theoretical calculations were performed using the unsteady aerodynamic lifting-surface method of Doublet Lattice. The trends of the Doublet Lattice data show an overall good comparison to both the steady and unsteady experimental aerodynamics. Comparisons for the steady data include chordwise incremental lifting-surface pressure distributions per incremental angle of attack and incremental control-surface deflection, spanwise incremental lift and moment distributions per incremental angle of attack, spanwise distributions of local aerodynamic center locations, and spanwise incremental lift distributions per incremental inboard and outboard control-surface deflection. The theoretical and experimental lifting-surface unsteady-pressure

coefficient magnitude and phase angle comparisons are show. for both inboard and outboard oscillating control surfaces.

Although, in general, the experimental and theoretical data show reasonably good agreement, there are some significant areas of deviation. These differences, which could possibly be adjusted with empirically-developed correction factors, are noted as follows:

1. The Doublet Lattice data underpredicts experimental chordwise steady-pressure distributions toward the leading edge and overpredicts values toward the trailing edge. This deviation is typical of thickness effects (viscosity) as discussed in ref. 8.

2. The most significant deviation is the Doublet Lattice overprediction of experimental chordwise pressure distributions on the control surfaces. The difference in both steady- and unsteady-pressure magnitudes is more pronounced on the outboard control surface.

3. For the unsteady aerodynamics, the Doublet Lattice phase angle values are consistently more negative (lagging) than the experimental values toward the leading edge.

4. The experimental chordwise pressure distributions toward the trailing edge of the outboard control surface exhibited an effect possibly due to spanwise or separated flow. This is illustrated by a measured pressure rise at the trailing edge chordwise station $x/c = 0.95$ after a minimum pressure was reached forward of this location at $x/c = 0.90$.

REFERENCES

1. Peele, Ellwood L.; and Adams, William M., Jr.: A Digital Program for Calculating the Interaction Between Flexible Structures, Unsteady Aerodynamics and Active Controls. NASA TM 80040, 1979.

2. Adams, William M., Jr.; and Tiffany, Sherwood H.: Control Law Design to Meet Constraints Using SYNPAC--Synthesis Package for Active Controls. NASA TM 83264, 1982.

3. Miller, R. D.; Kroll, R. I.; and Clemmons, R. E.: Dynamic Loads Analysis System (DYLOFLEX) Summary. NASA CR-2846, 1979.

4. Perry, B., III; Kroll, R. I.; Miller, R. D.; and Goetz, R. C.: DYLOFLEX-A Computer Program for Flexible Aircraft Flight Dynamic Loads Analyses with Active Controls. J. of Aircraft, Vol. 17, April 1980, pp. 275-282.

5. Nissim, E.; and Abel, I.: Development and Application of an Optimization Procedure for Flutter Suppression Using the Aerodynamic Energy Concept. NASA TP 1137, 1978.

6. Sanford, Maynard C.; Ricketts, Rodney H.; and Cazier, F. W., Jr.: Transonic Steady- and Unsteady-Pressure Measurements on a High-Aspect-Ratio Supercritical-Wing Model with Oscillating Control Surfaces. NASA TM 81888, 1980.

7. Sanford, Maynard C.; Ricketts, Rodney H.; and Watson, Judith J.: Subsonic and Transonic Pressure Measurements on a High-Aspect-Ratio Supercritical-Wing Model with Oscillating Control Surfaces. NASA TM 83201, 1981.

8. Rowe, W. S.; Redman, M. C.; Ehlers, F. E.; and Sebastian, J. D.: Prediction of Unsteady Aerodynamic Loadings Caused by Leading Edge and Trailing Edge Control Surface Motions in Subsonic Compressible Flow--Analysis and Results. NASA CR-2543, 1975.

9. Rowe, W. S.; Sebastian, J. D.; and Petrarca, J. R.: Reduction of Computer Usage Costs in Predicting Unsteady Aerodynamic Loadings Caused by Control Surface Motions--Analysis and Results. NASA CR-3009, 1979.

10. Bland, S. R.: Recent Advances and Concepts in Unsteady Aerodynamic Theory. NASA SP-347, Pt. II, 1975, pp. 1305-1326.

11. Broadbent, E. G.: Some Recent Development in Aeronautical Fluid Mechanics, RAE Tech. Memo. Aero 1894, March 1981.

12. Caughey, D. A.: The Computation of Transonic Potential Flows. Annual Review of Fluid Mechanics, Vol. 14, 1982, pp. 261-283.

13. Abel, I.; Perry, B, III; and Newsom, J. R.: Comparison of Analytical and Wind-Tunnel Results for Flutter and Gust Response of a Transport Wing with Active Controls. NASA TP 2010, 1982.

14. Watson, Judith J.: Elastic Deformation Effects on Aerodynamic Characteristics for a High-Aspect-Ratio Supercritical-Wing Model. NASA TM 83286, 1982.

15. Giesing, J. P.; Kalman, T. P.; and Rodden, W. P.: Subsonic Unsteady Aerodynamics for General Configurations, Part I. Direct Application of the Nonplanar Doublet Lattice Method. AFFDL-TR-71-5, Vol. I, November 1971.

TABLE I. - SUMMARY OF EXPERIMENTAL STEADY-PRESSURE TEST CONDITIONS AT M = 0.60

Test Point No. (See Ref. 7)	α deg	δ deg
Inboard Control Surface		
265	0	+ 6
266		+ 4
267		+ 2
268		- 2
269		- 4
270		- 6
271		0
186	2.84	+ 6
187		+ 4
188		+ 2
190		- 2
191		- 4
192		- 6
193		0
Outboard Control Surface		
218	0	+ 6
219		+ 4
222		+ 2
223		- 2
224		- 4
225		- 6
226		0
174	2.85	+ 6
161		+ 4
175		+ 2
178		- 2
162		- 4
184		- 6
185		0

TABLE II. - SUMMARY OF EXPERIMENTAL UNSTEADY-PRESSURE TEST CONDITIONS AT M = 0.60

Test Point No. (See Ref. 7)	α deg	δ deg	f Hz	k
Inboard Control Surface				
121	0	± 4	5	0.135
124	⎜	⎜	10	0.272
125	⎜	⎜	15	0.408
145	2.85	⎜	5	0.136
144	2.85	⎜	10	0.272
143	2.84	⎜	15	0.408
Outboard Control Surface				
130	0	± 4	5	0.136
129	⎜	⎜	10	0.273
128	⎜	⎜	15	0.410
139	2.84	⎜	5	0.136
140	2.84	⎜	10	0.272
142	2.84	⎜	15	0.408

Orifice Row No.	Semispan Stations η
1	0.19
2	0.23
3	0.25
4	0.33
5	0.51
6	0.71
7	0.78
8	0.81
9	0.92

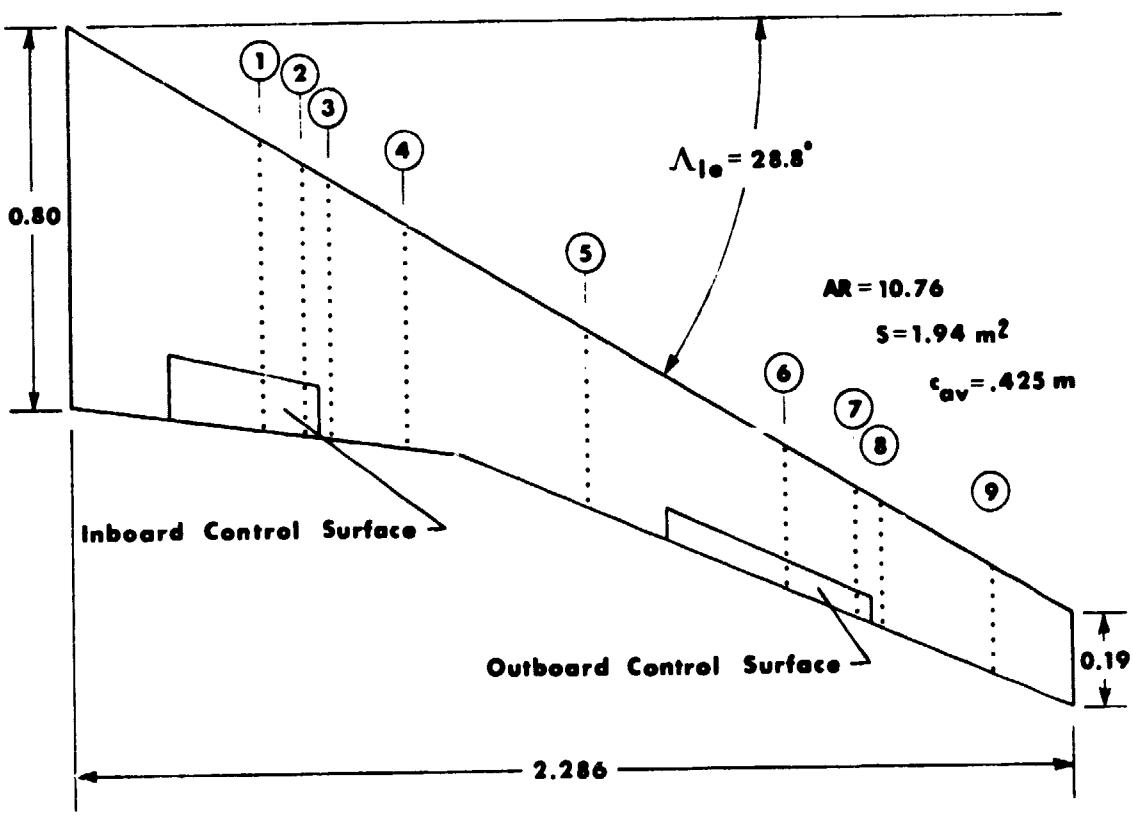

Figure 1. - Sketch of wing planform geometry and orifice semispan stations. Linear dimensions in meters.

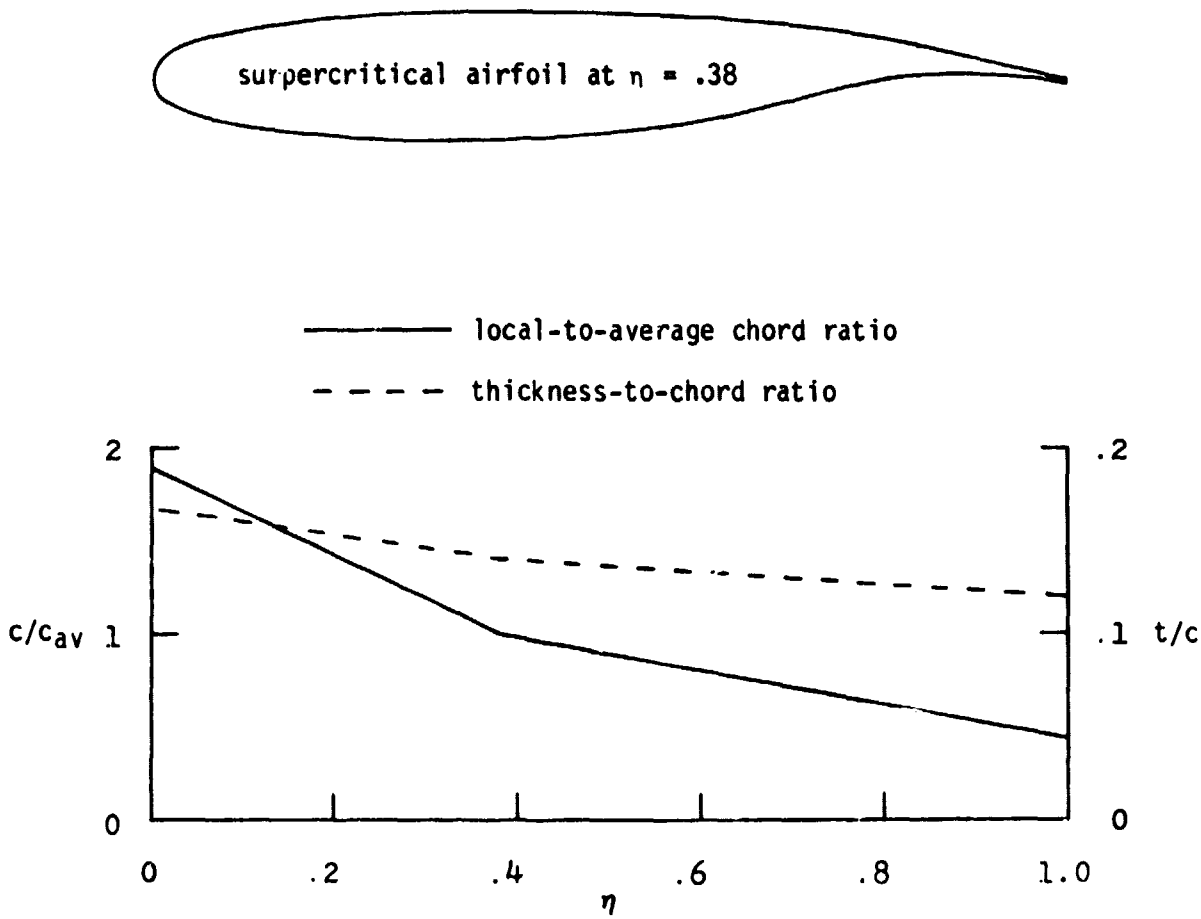

Figure 2.- Sketch of supercritical airfoil for 3-dimensional wind-tunnel model and plot of local chord and thickness variation along semispan.

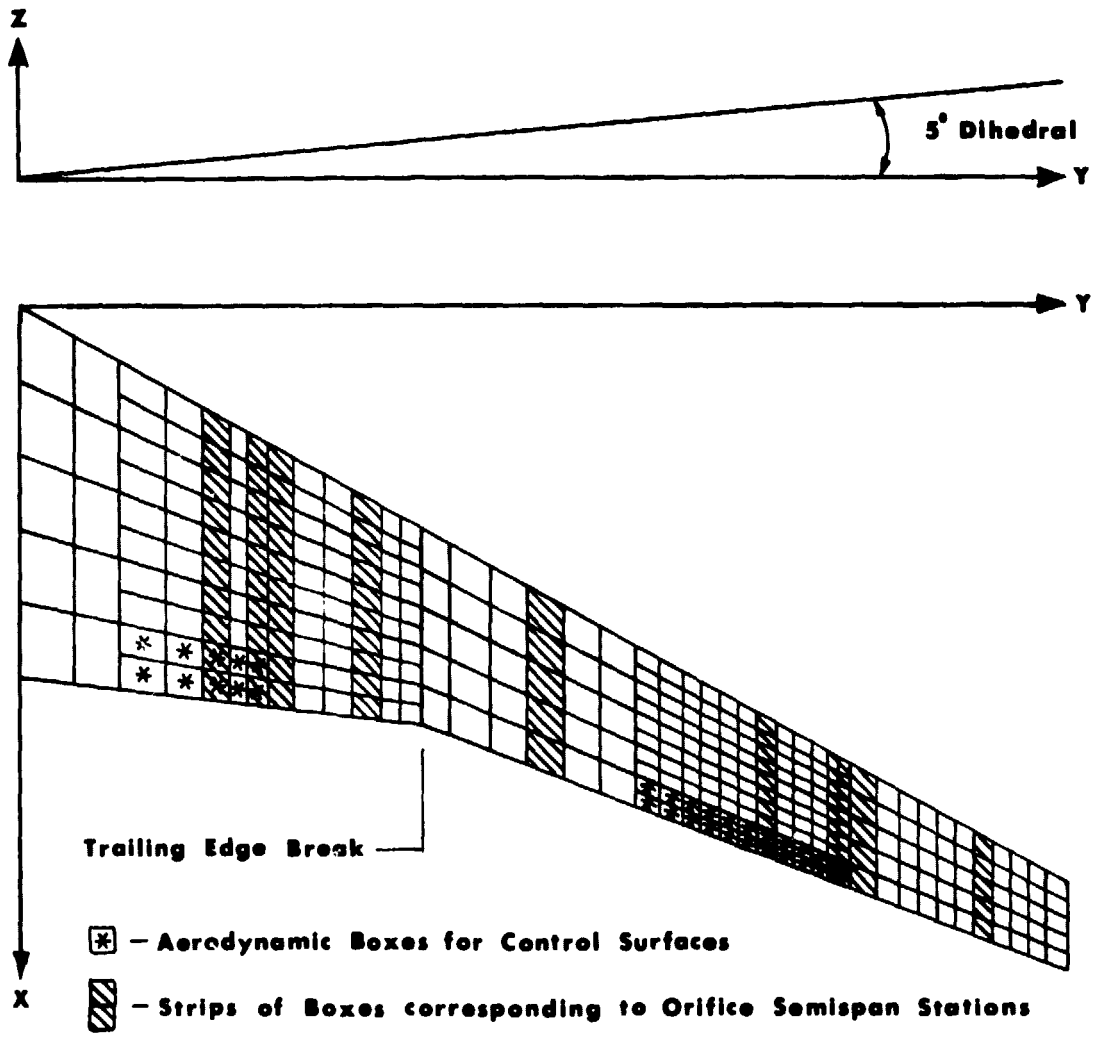

Figure 3.- Sketch of Doublet Lattice aerodynamic model.

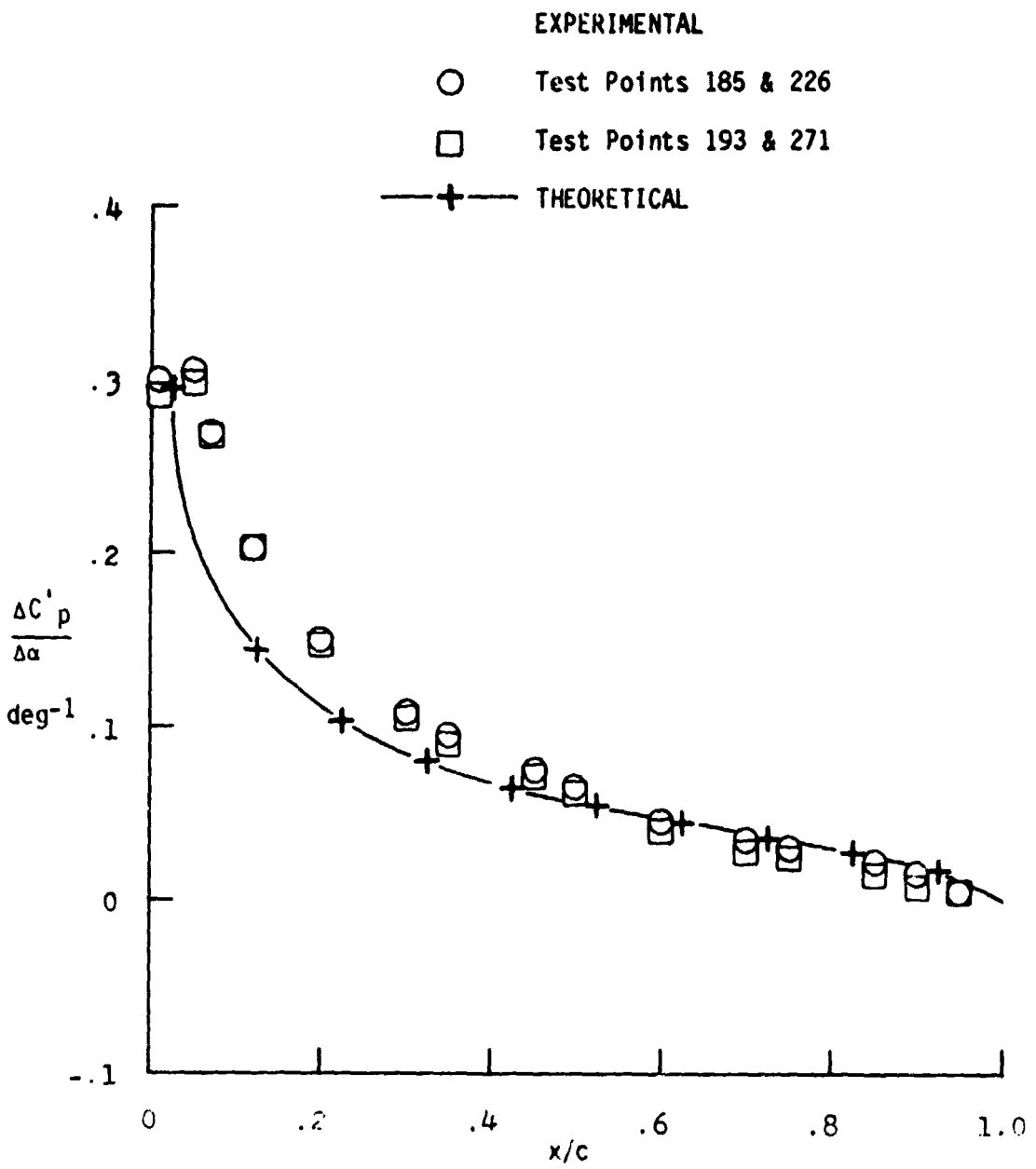

(a) At semispan location η = 0.19.

Figure 4. - Chordwise incremental lifting-surface steady-pressure distribution for an incremental angle of attack.

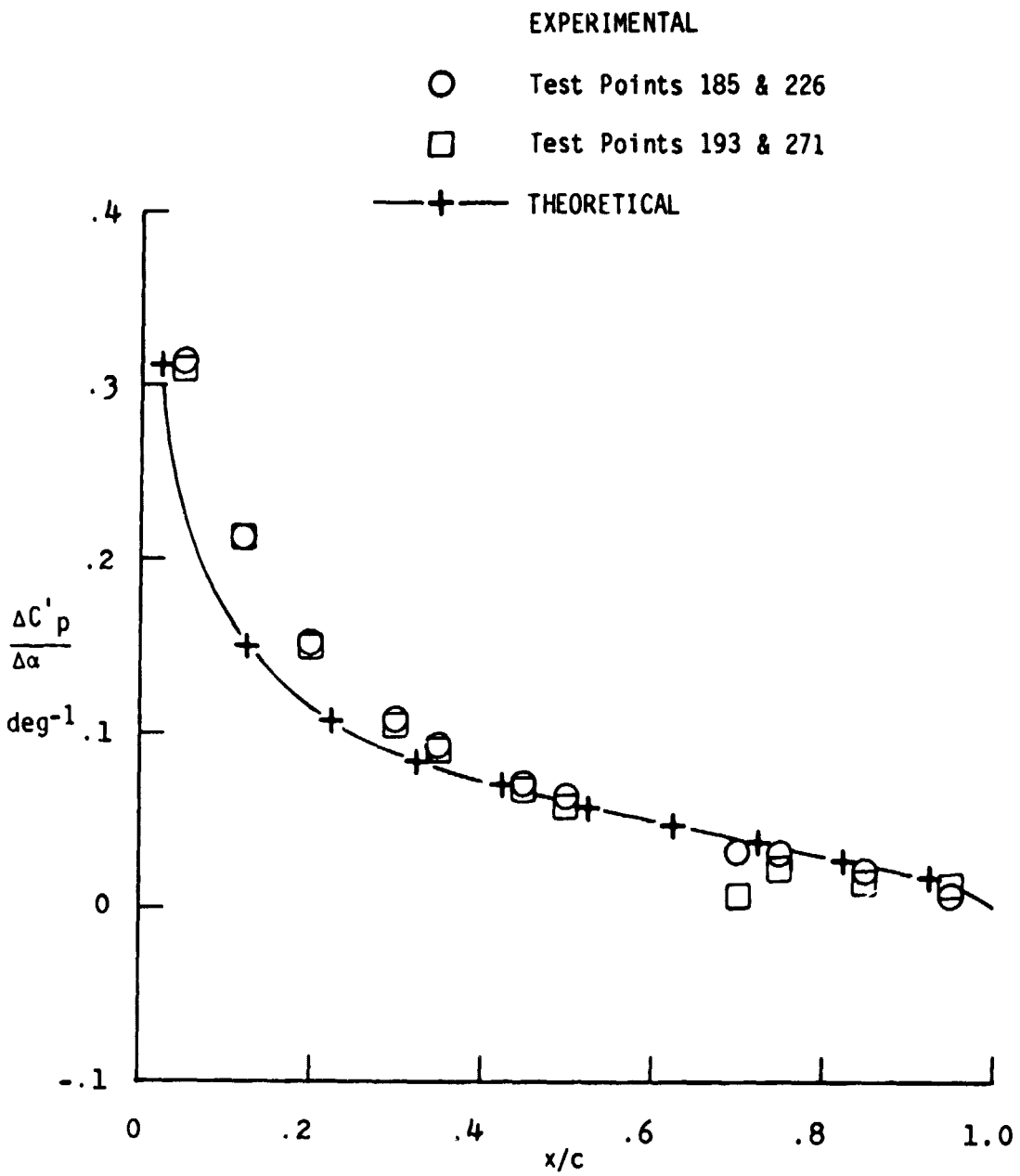

(b) At semispan loaction n = 0.23.

Figure 4.- Continued.

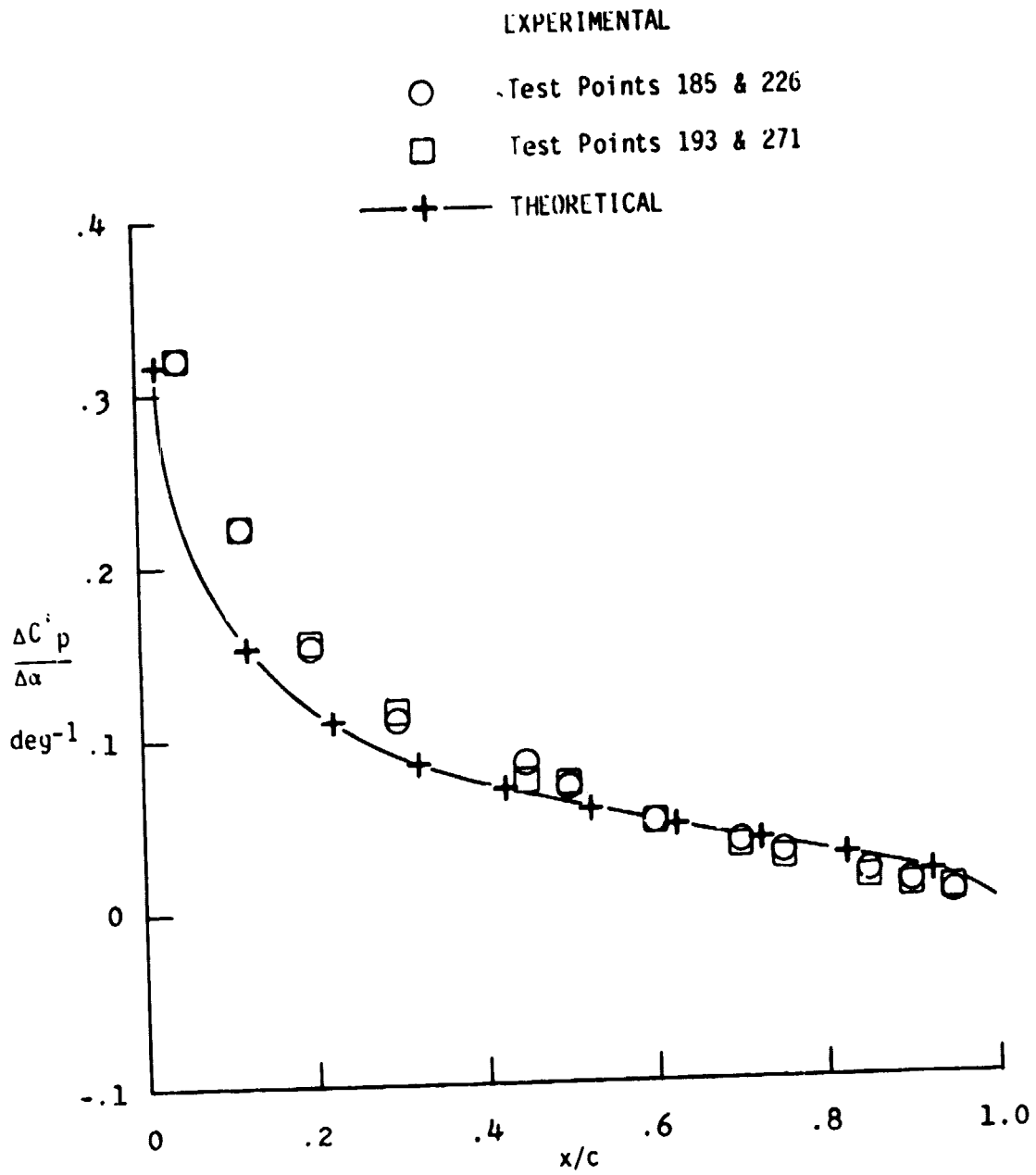

(c) At semispan location n = 0.25.

Figure 4.- Continued.

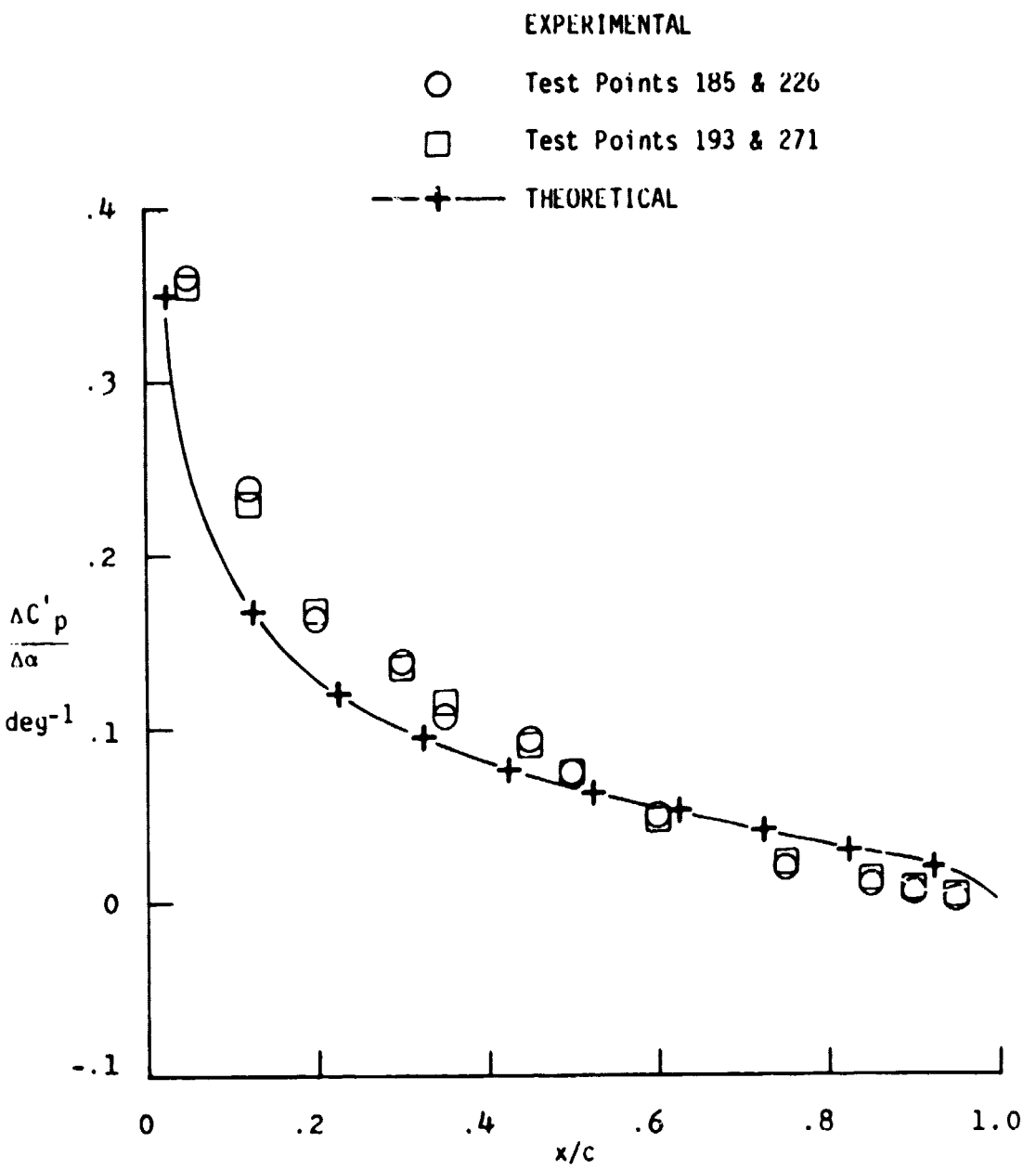

(d) At semispan location η = 0.33.

Figure 4.- Continued.

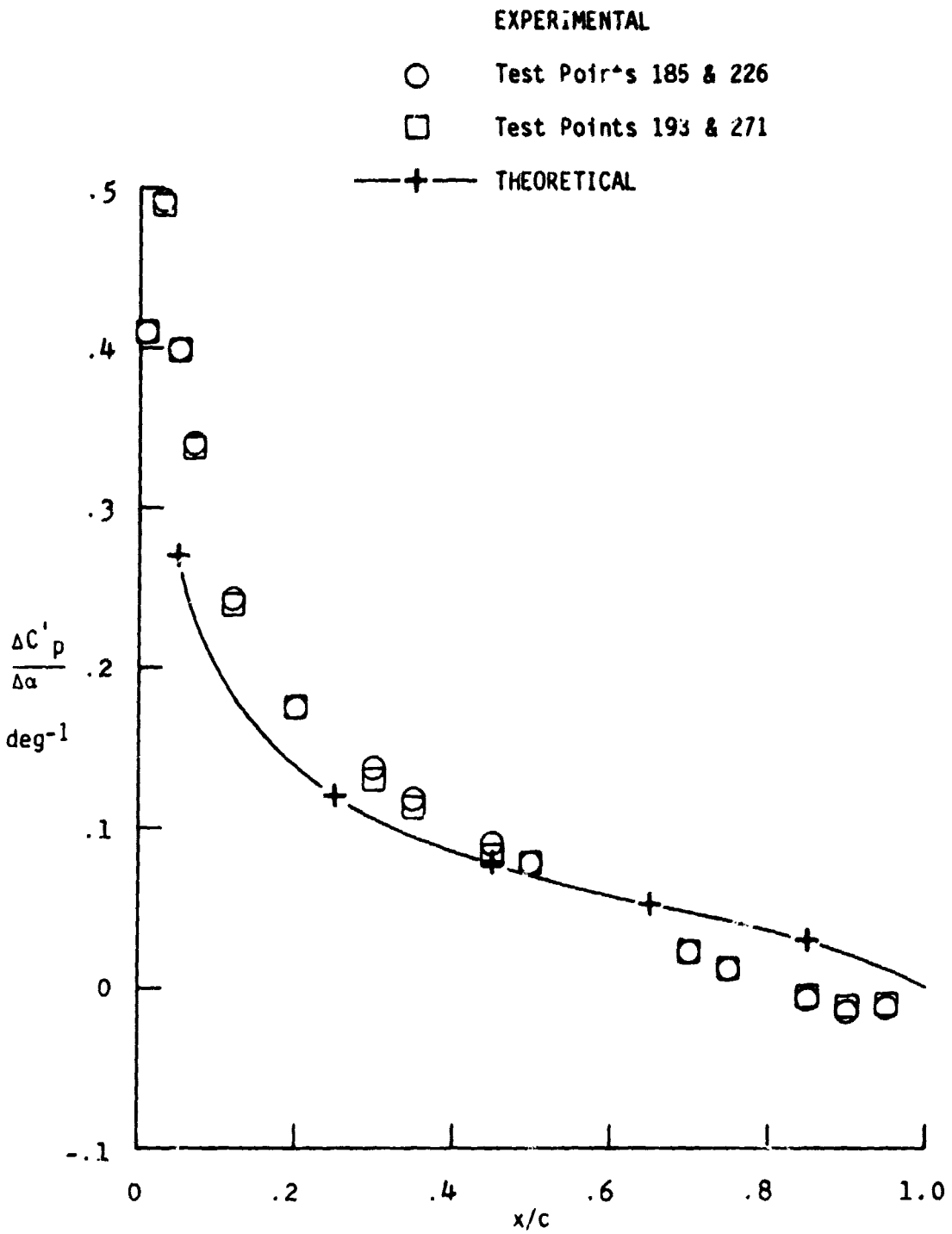

(e) At semispan location η = 0.51.

Figure 4.- Continued.

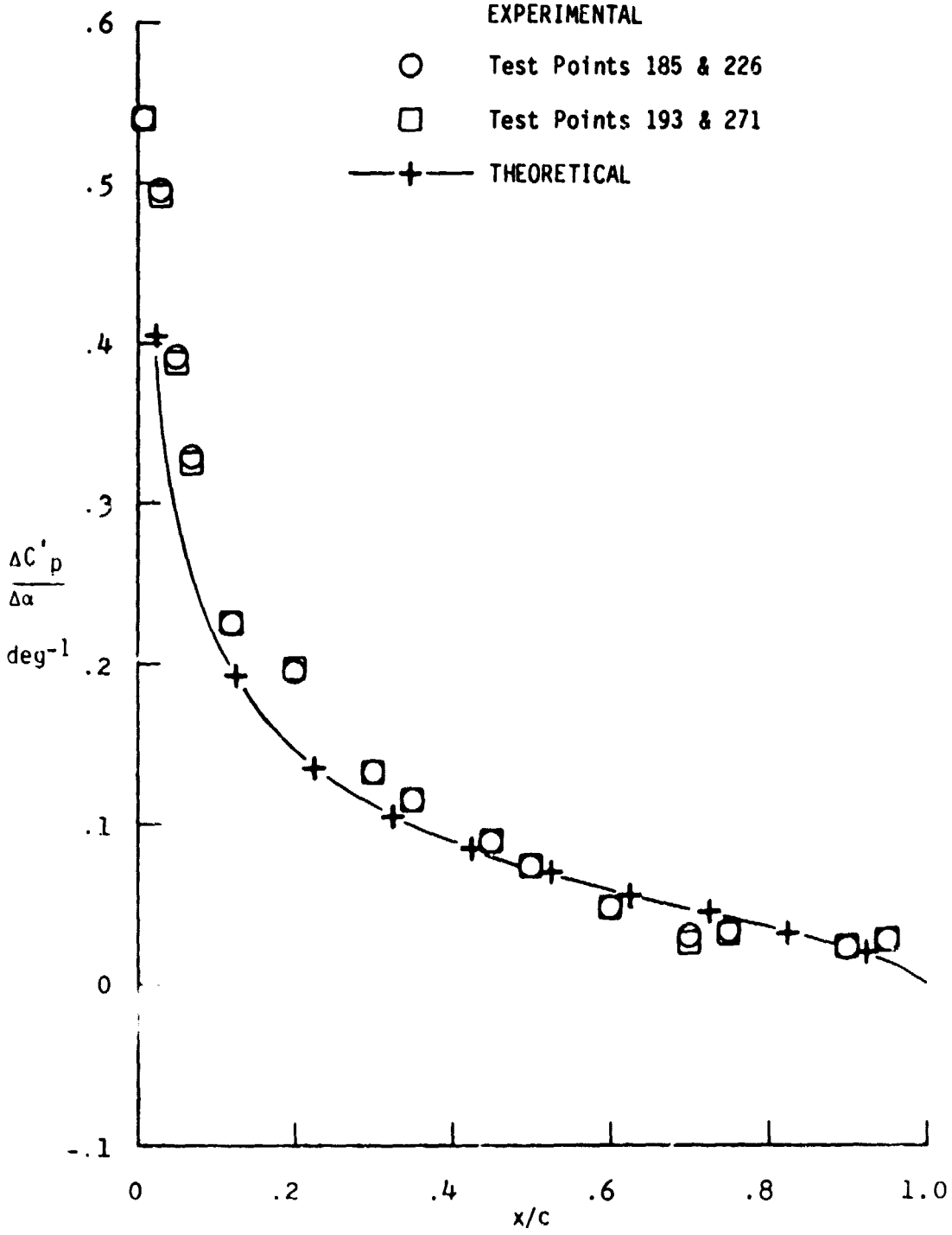

(f) At semispan location $\eta = 0.71$.

Figure 4.- Continued.

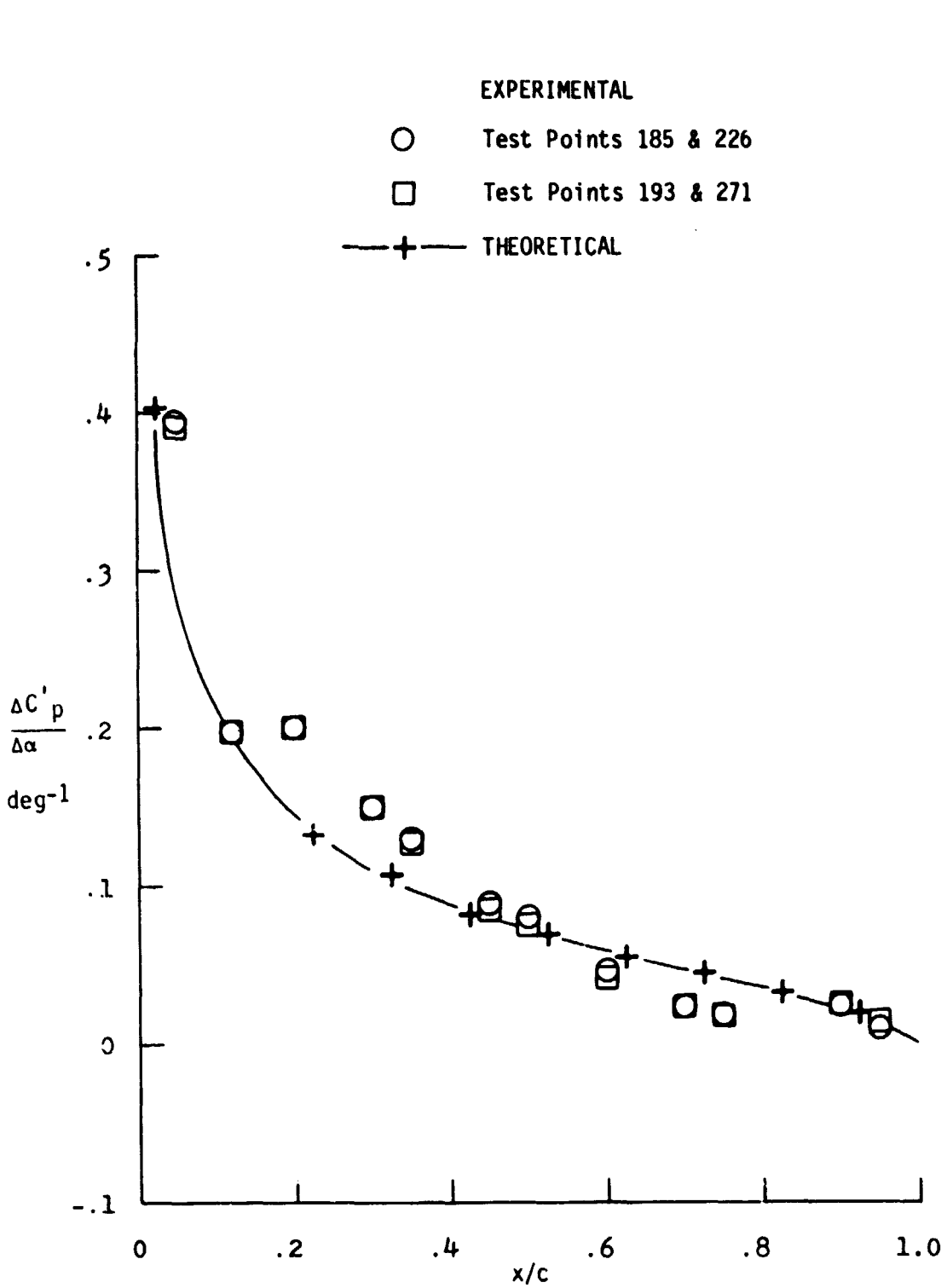

(g) At semispan location $\eta = 0.78$.

Figure 4.- Continued.

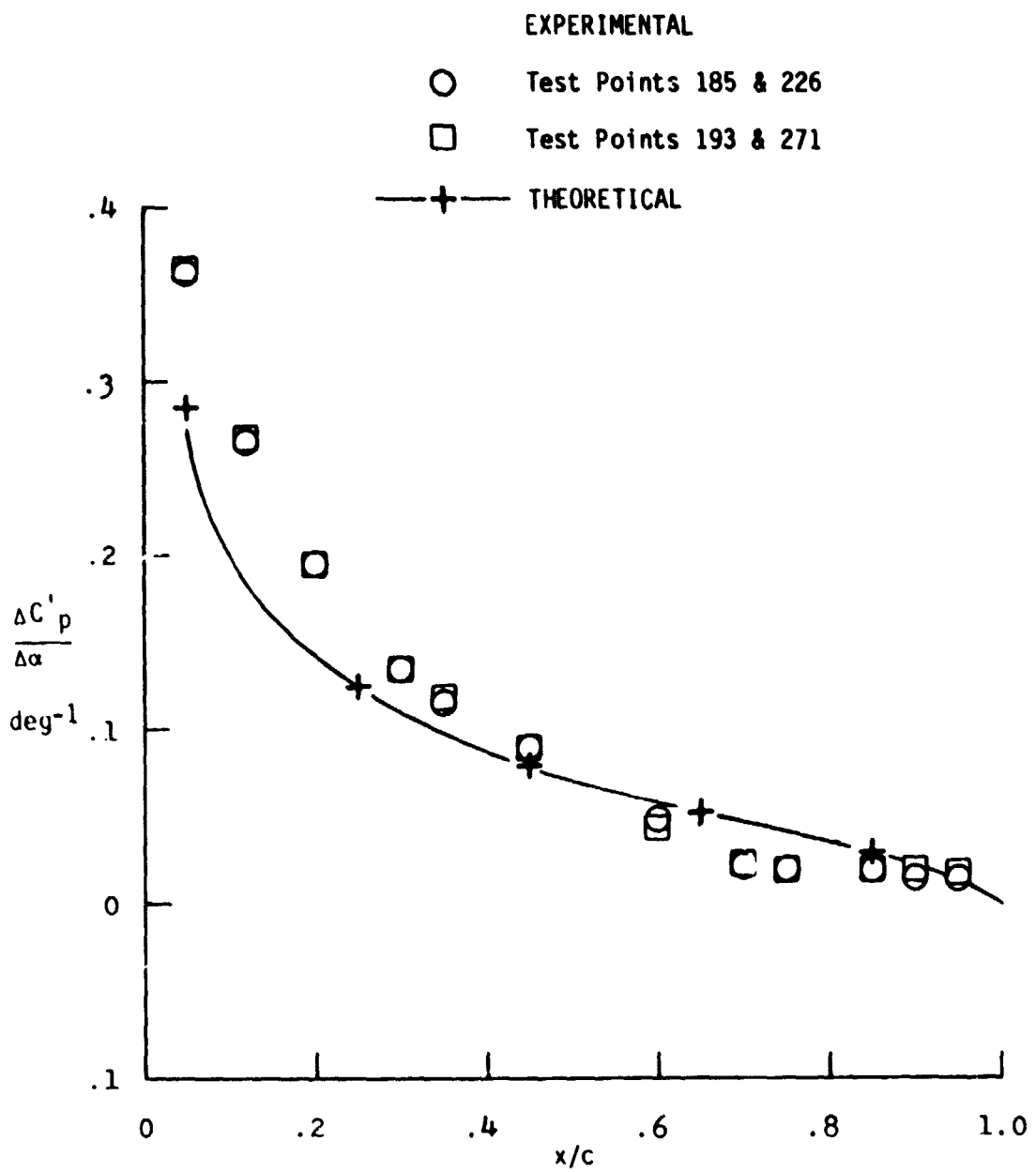

(h) At semispan location η = 0.81.

Figure 4.- Continued.

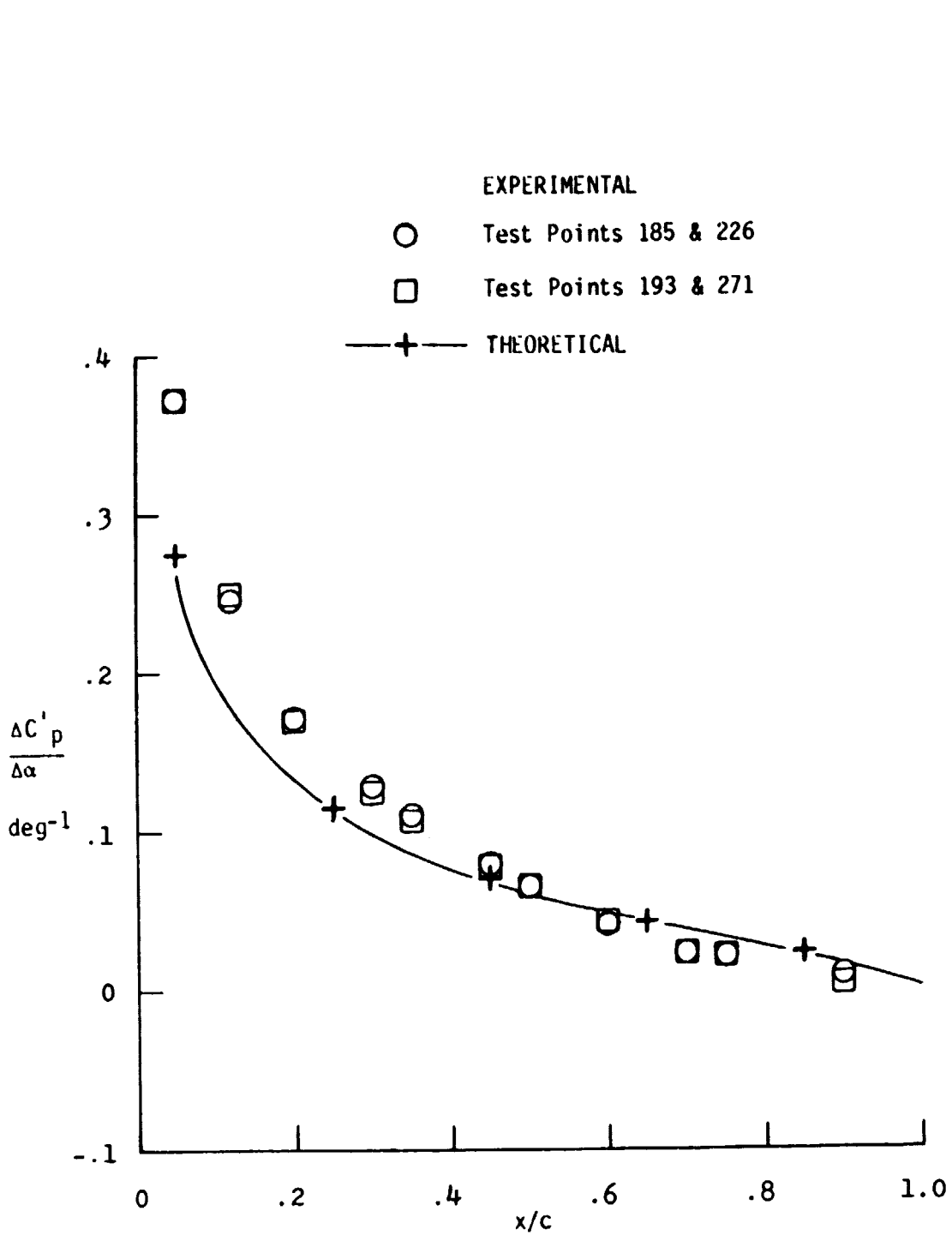

(i) At semispan location n = 0.92.

Figure 4.- Concluded.

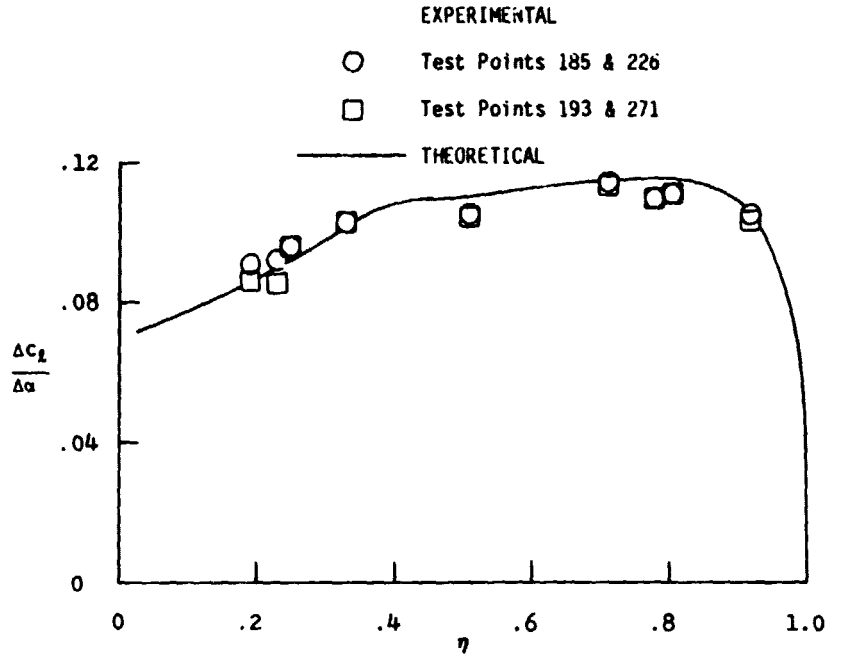

(a) Incremental section lift coefficient.

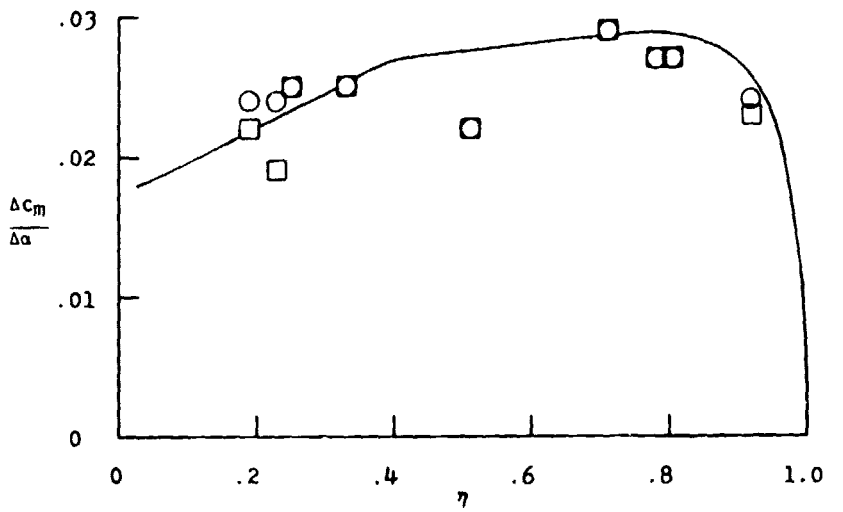

(b) Incremental section pitching-moment coefficient.

Figure 5. - Spanwise lift and moment distributions for an incremental angle of attack.

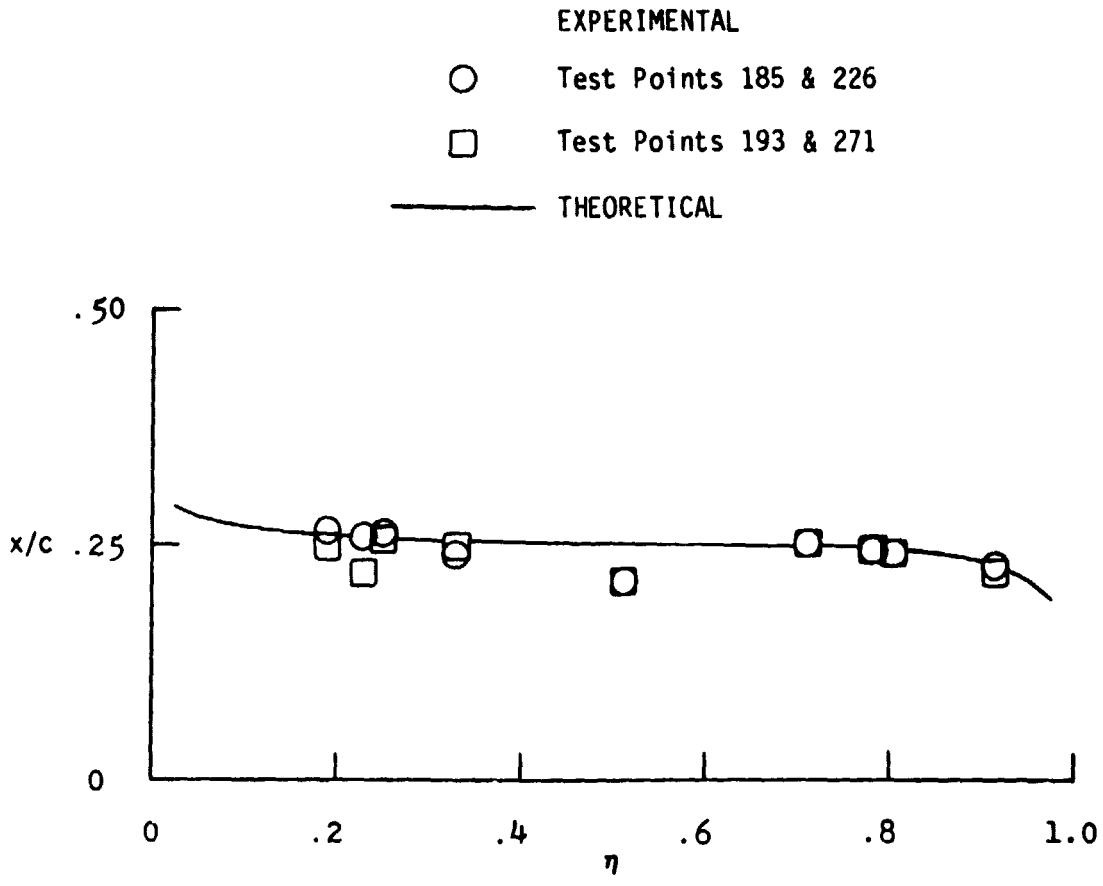

Figure 6. - Spanwise distribution of local aerodynamic center locations.

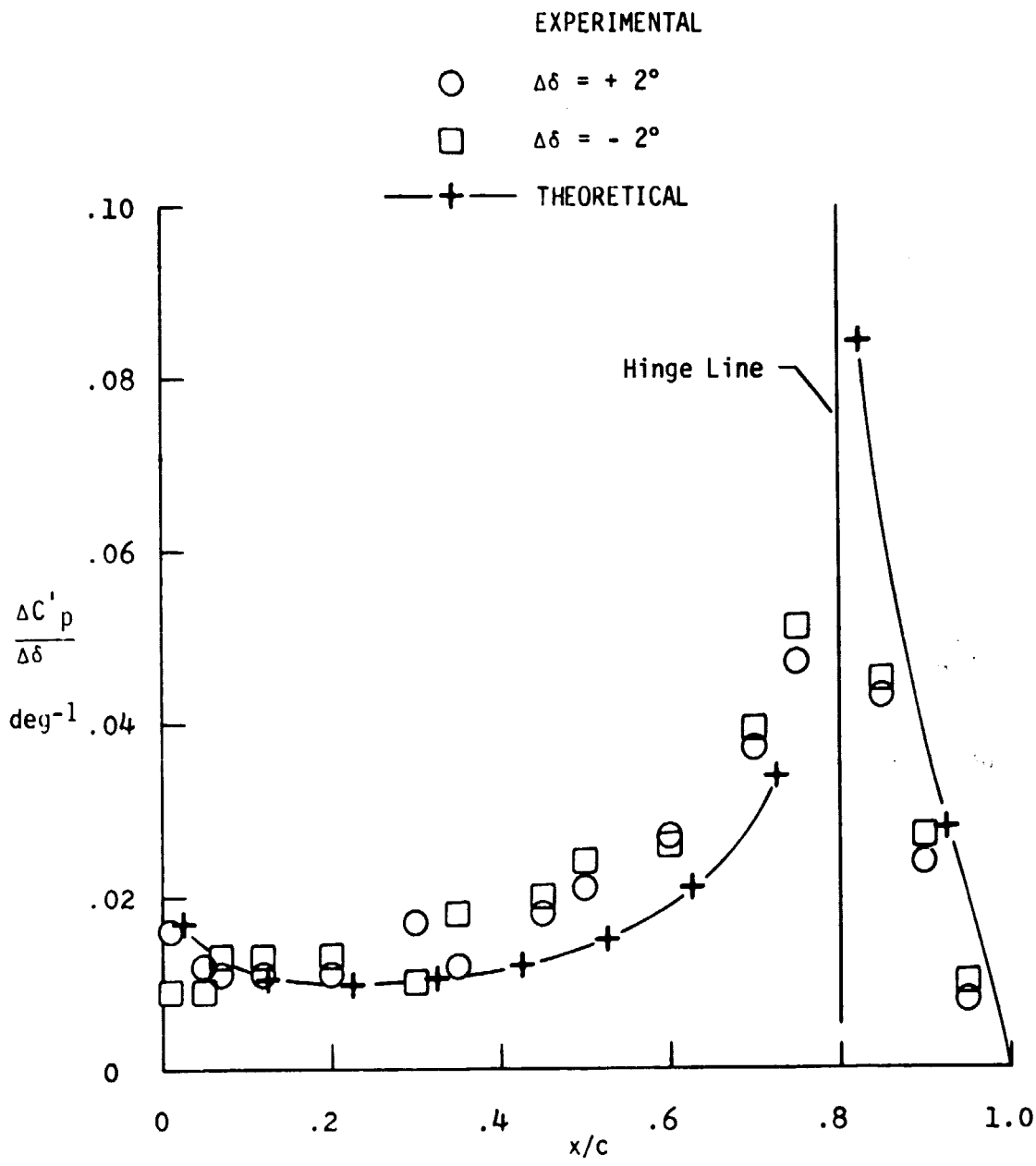

(a) For $\Delta\delta = \pm 2°$ and $\alpha = 0°$.

Figure 7. - Chordwise incremental lifting-surface steady-pressure distribution for an incremental inboard control-surface deflection at semispan station $\eta = 0.19$.

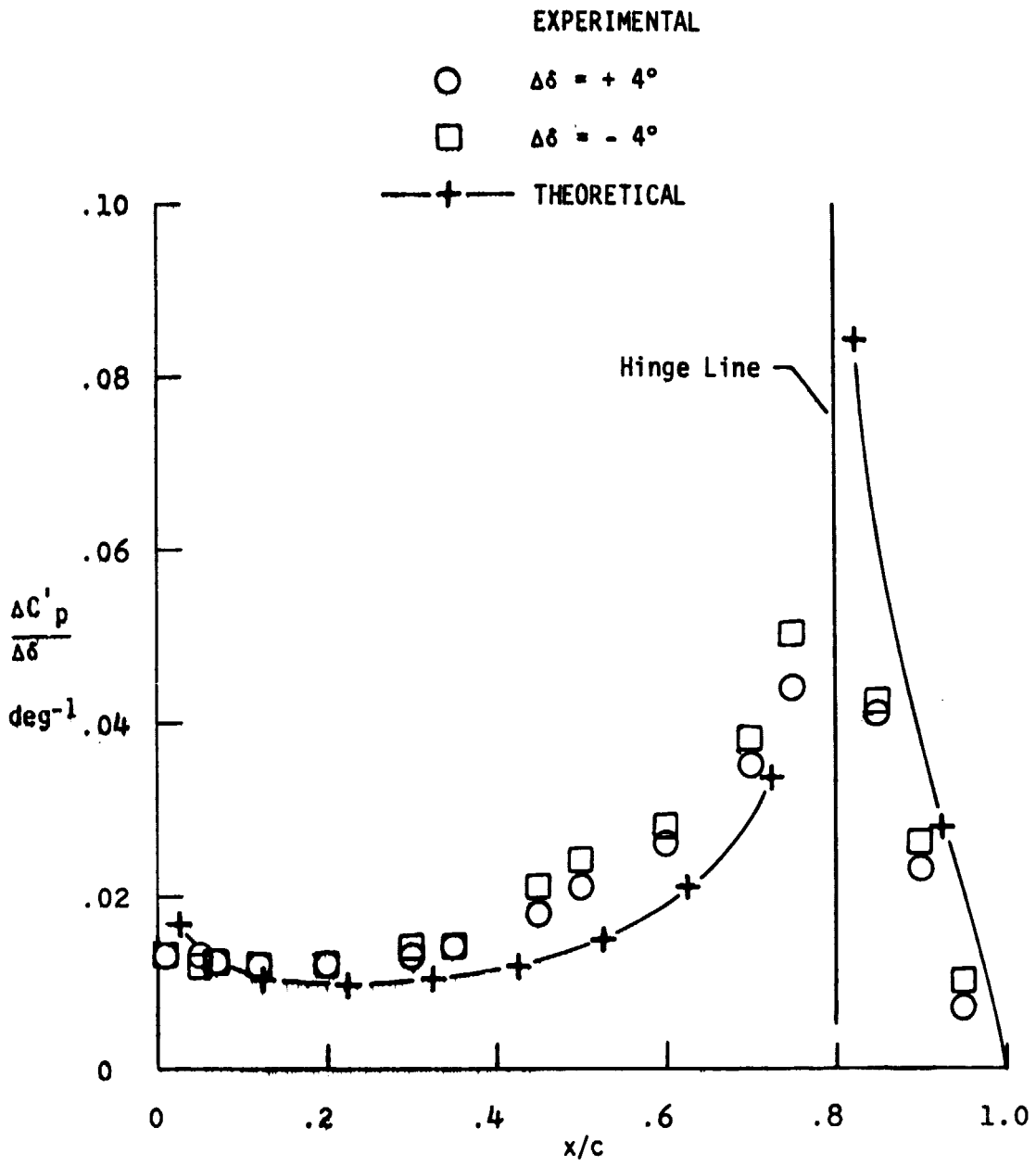

(b) For $\Delta\delta = \pm 4°$ and $\alpha = 0°$.

Figure 7.- Continued.

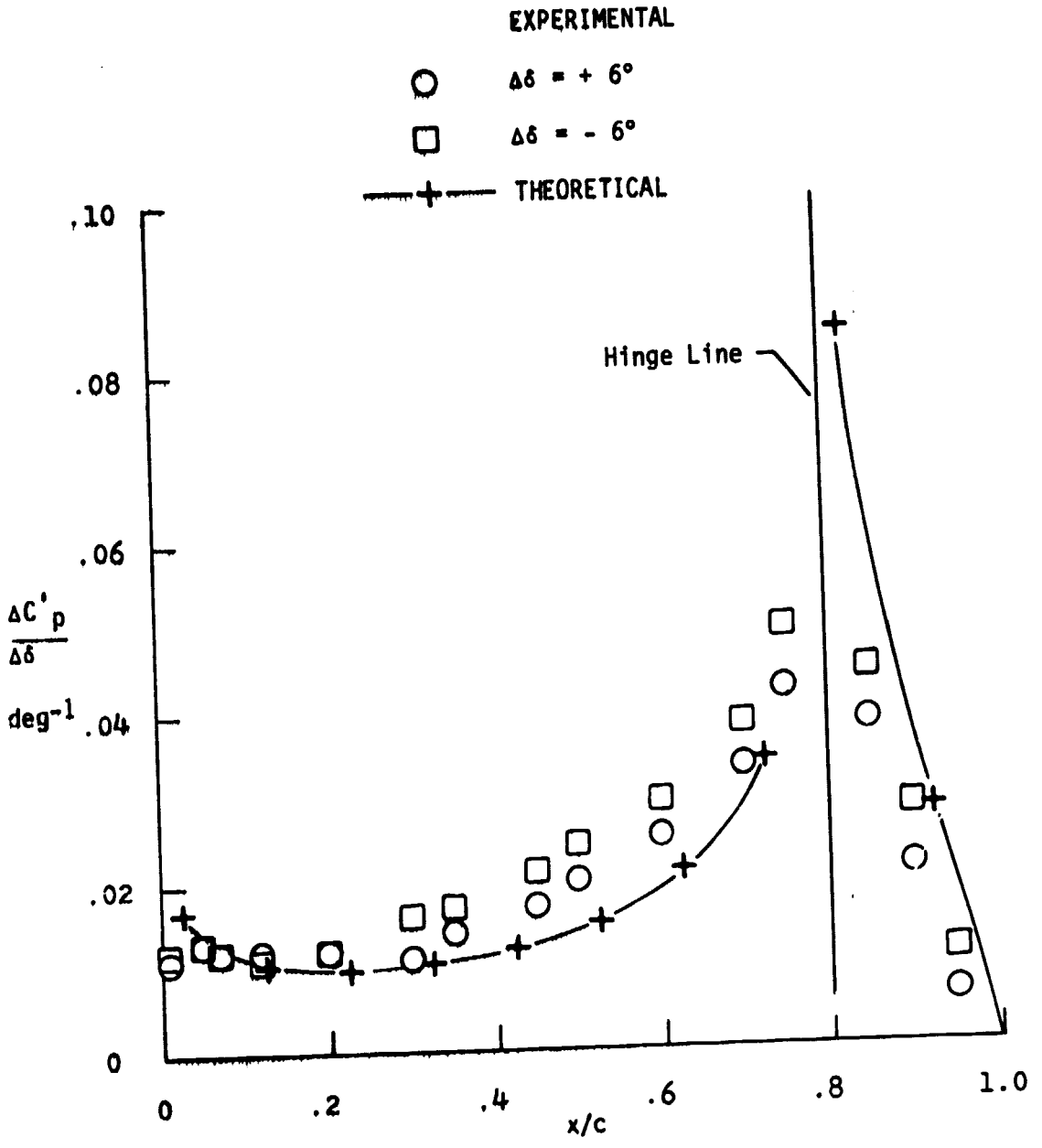

(c) For $\Delta\delta = \pm 6°$ and $\alpha = 0°$.

Figure 7.- Continued.

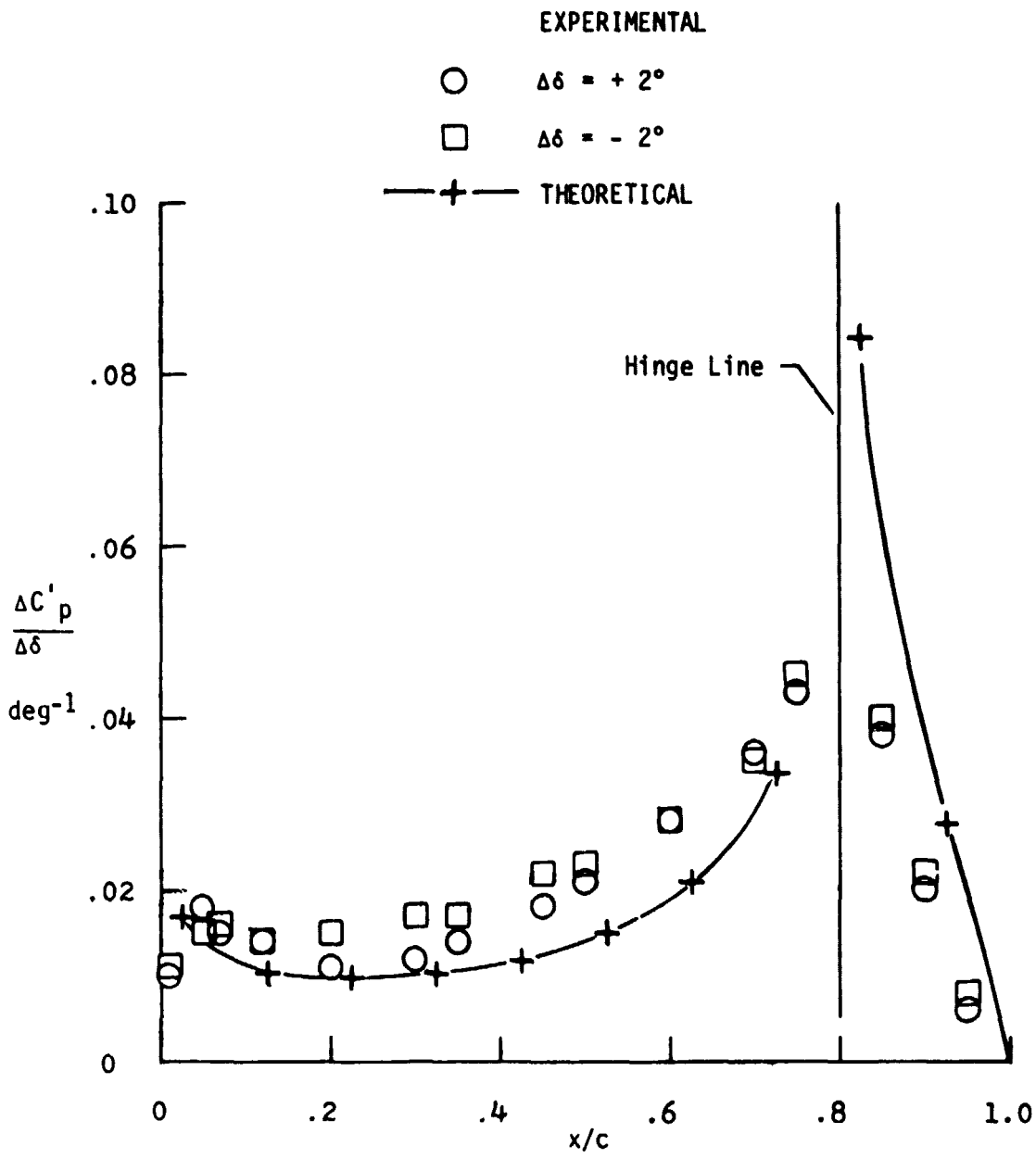

(d) For $\Delta\delta = \pm$ [illegible]° and $\alpha = 2.84°$.

Figure 7.- Continued.

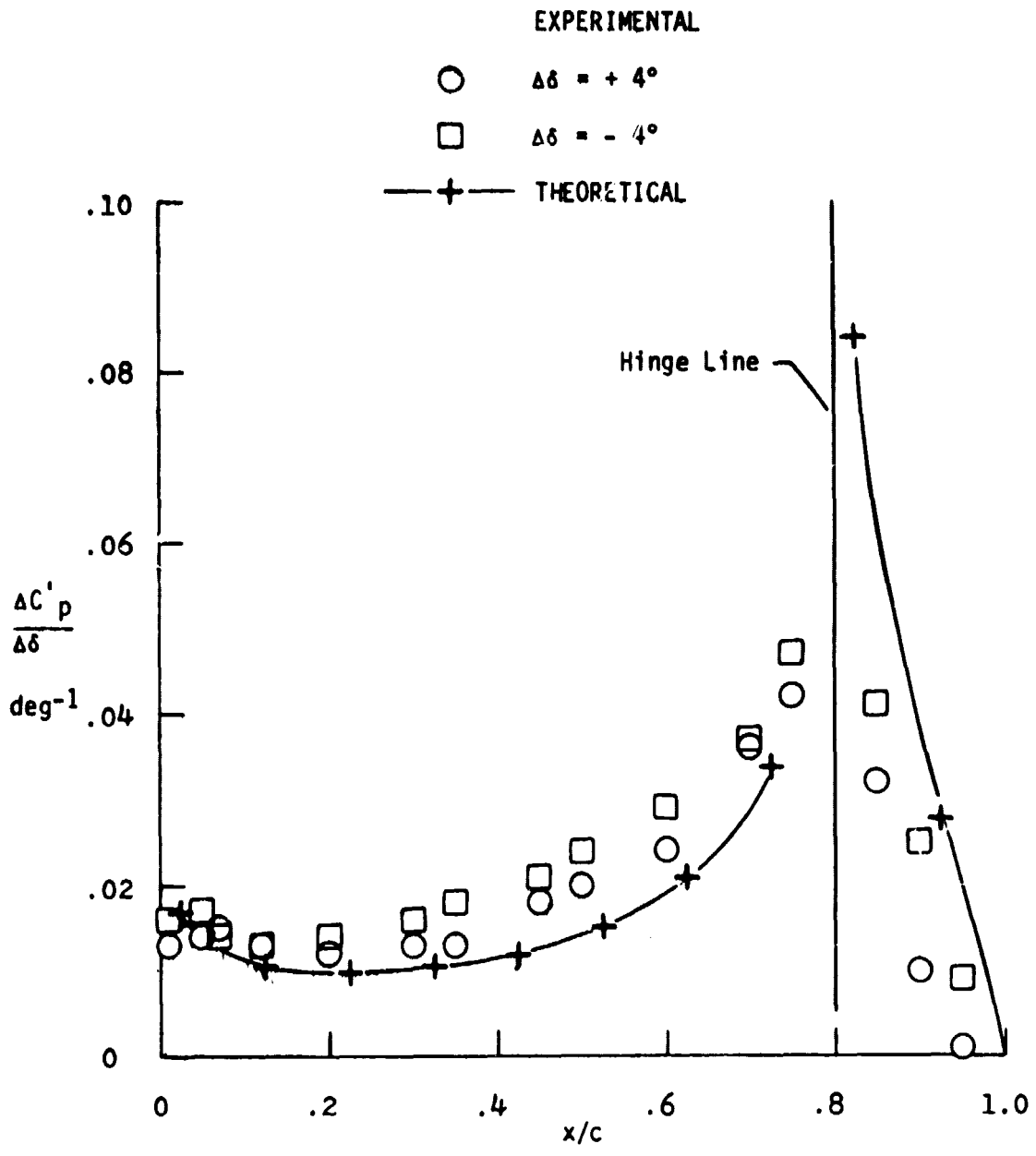

(e) For $\Delta\delta = \pm 4°$ and $\alpha = 2.84°$.

Figure 7.- Continued.

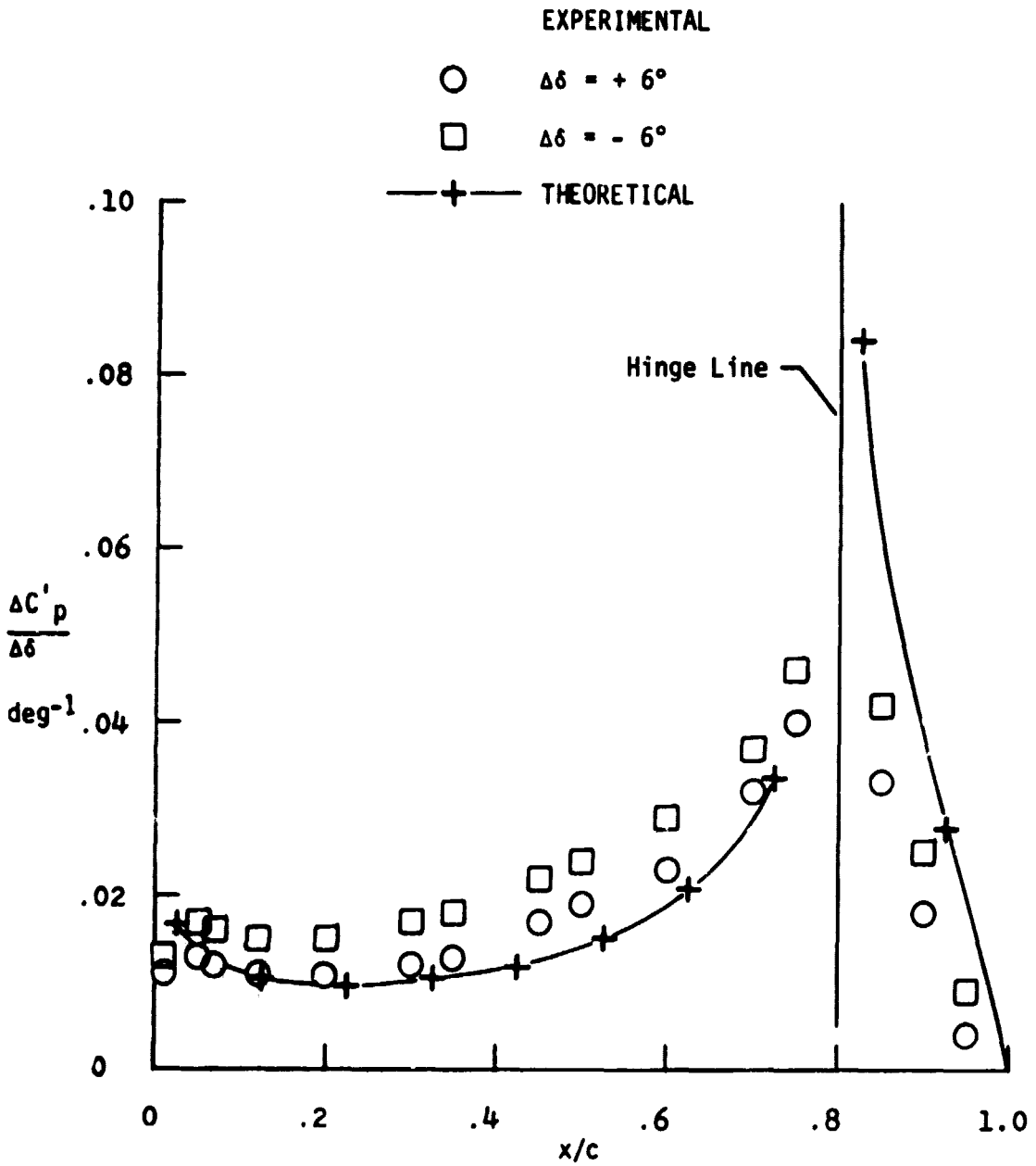

(f) For $\Delta\delta = \pm 6°$ and $\alpha = 2.84°$.

Figure 7.- Concluded.

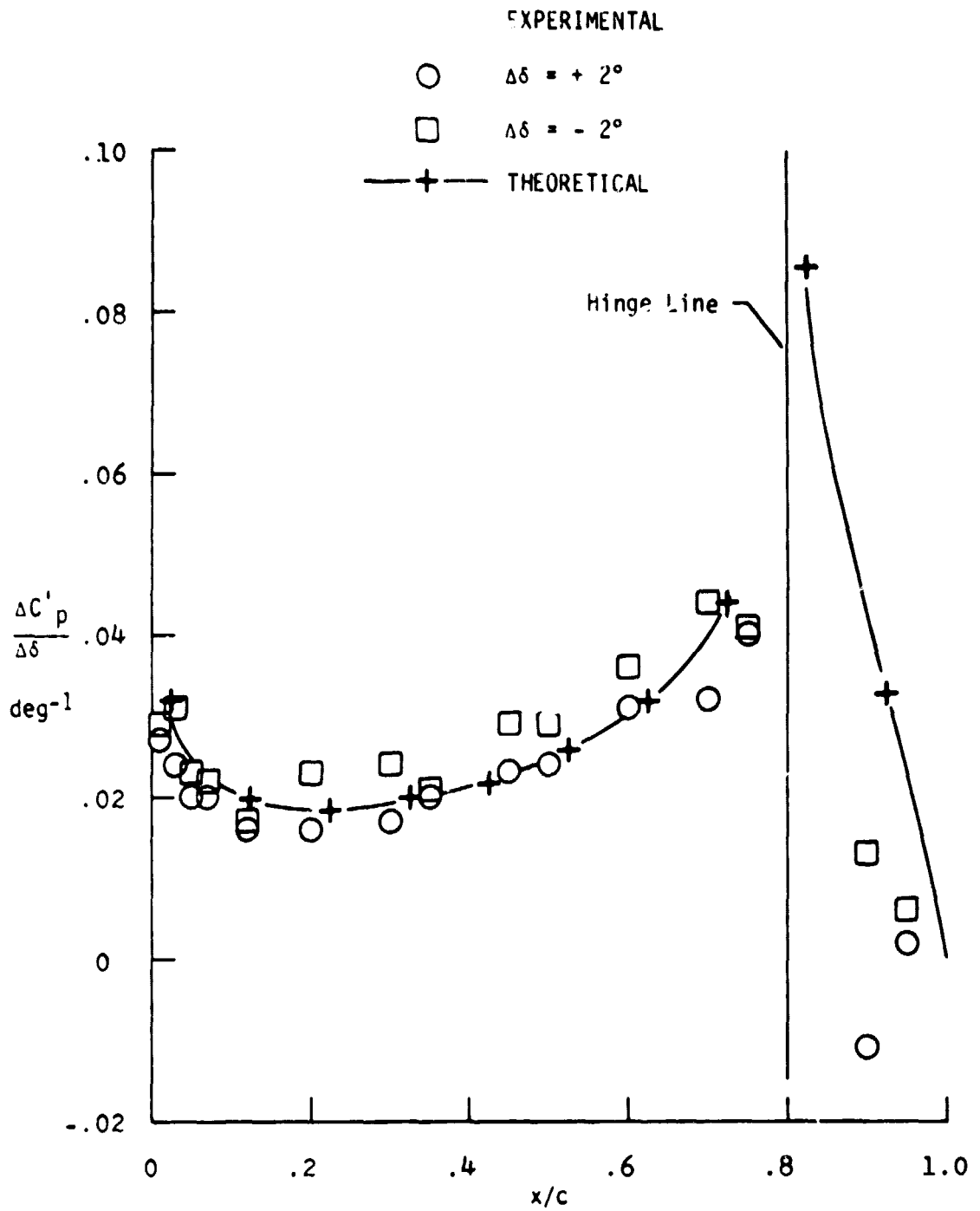

(a) For $\Delta\delta = \pm 2°$ and $\alpha = 0°$.

Figure 8. - Chordwise incremental lifting-surface steady-pressure distribution for an incremental outboard control-surface deflection at semispan station $\eta = 0.71$.

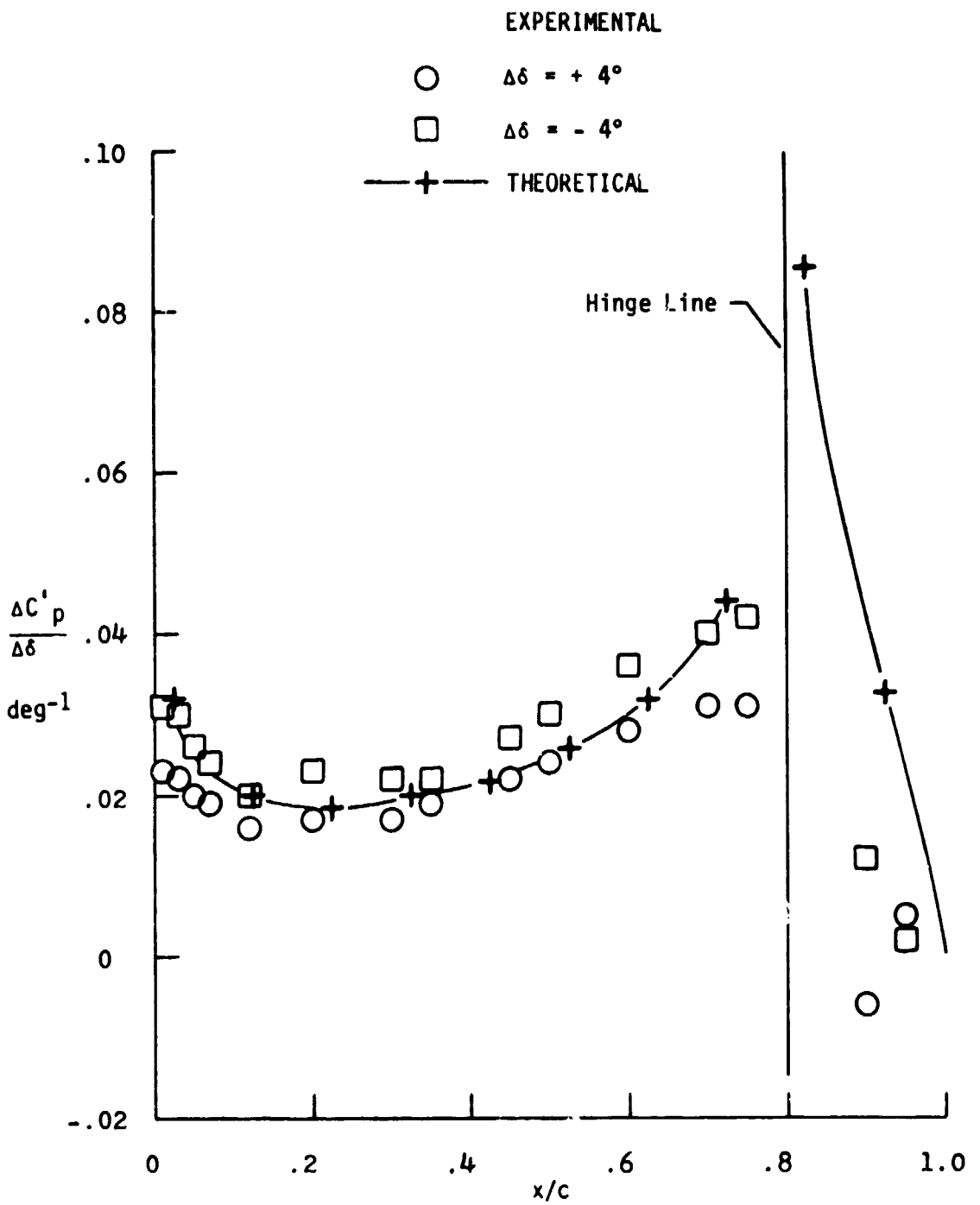

(b) For $\Delta\delta = \pm 4°$ and $\alpha = 0°$.

Figure 8.- Continued.

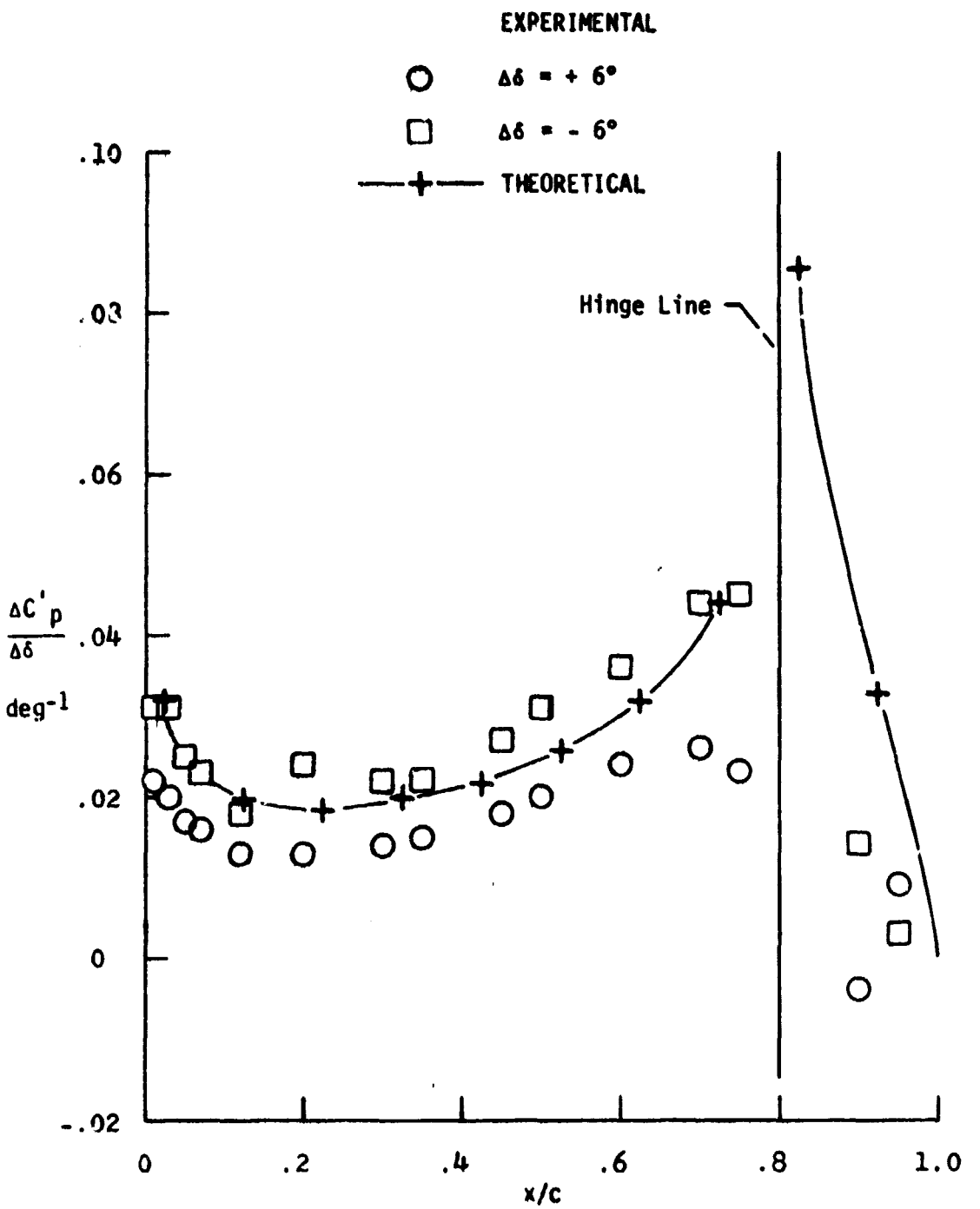

(c) For $\Delta\delta = \pm 6°$ and $\alpha = 0°$.

Figure 8.- Continued.

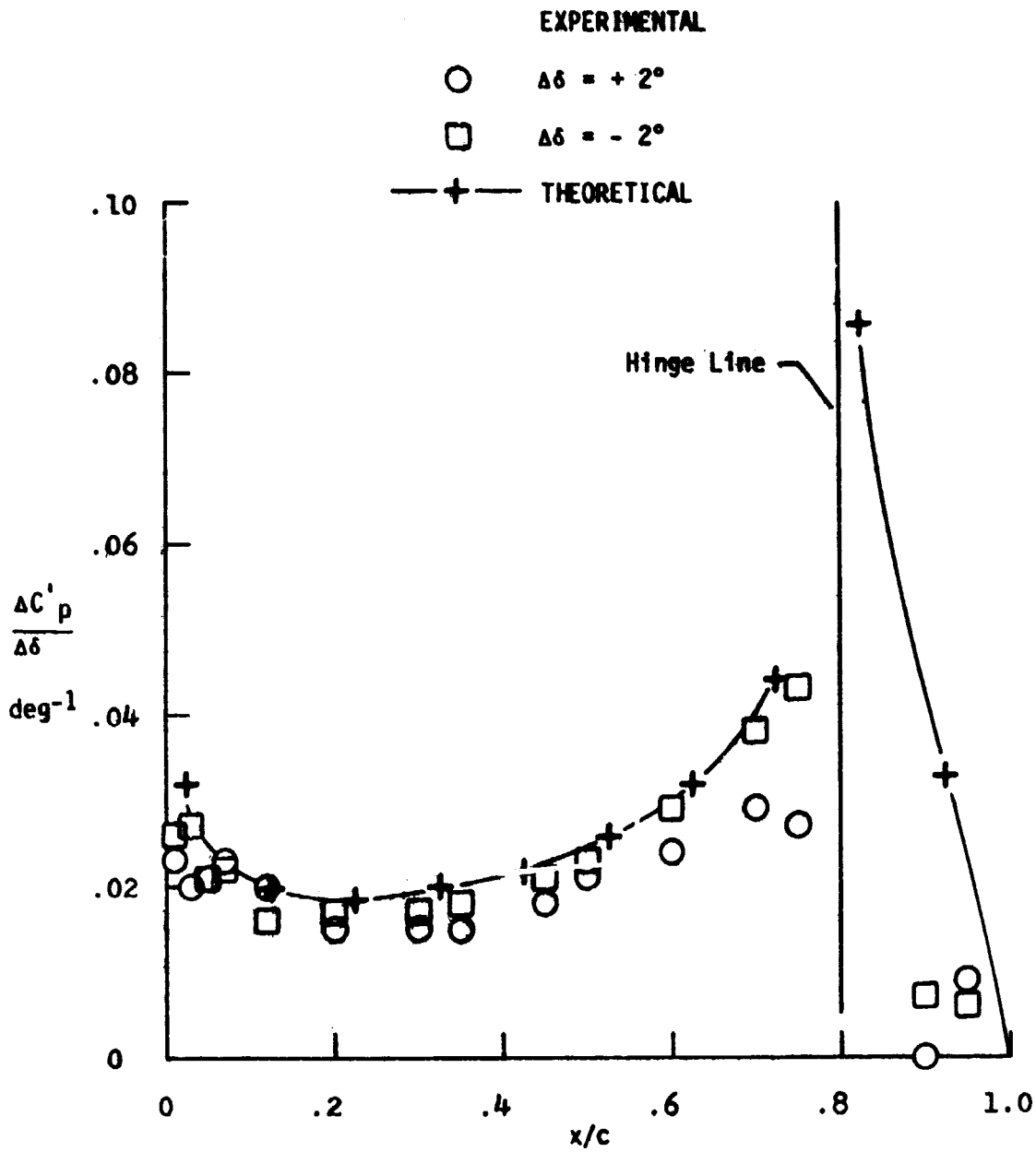

(d) For $\Delta\delta = \pm 2°$ and $\alpha = 2.85°$.

Figure 8.- Continued.

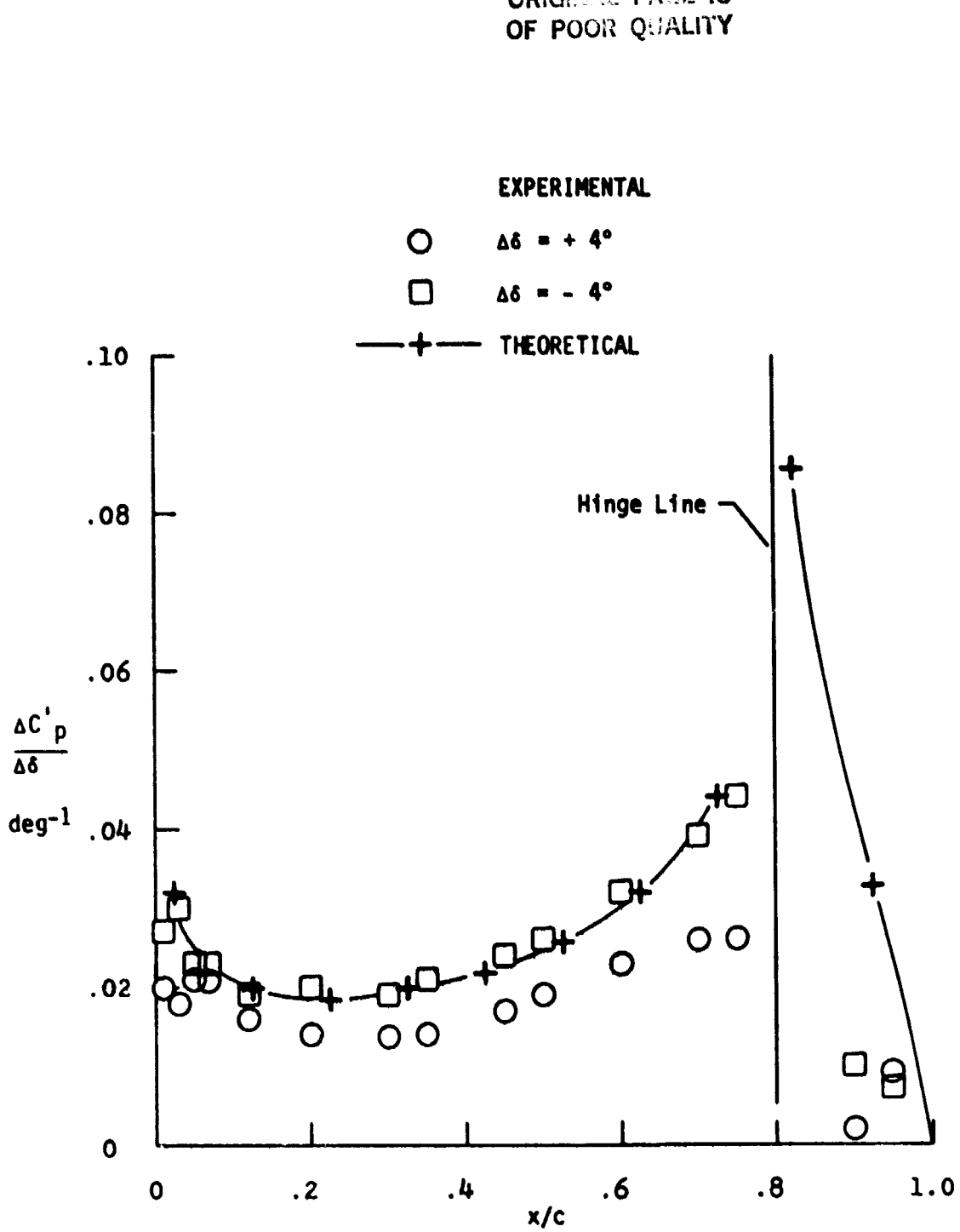

(e) For $\Delta\delta = \pm 4°$ and $\alpha = 2.85°$.

Figure 3.- Continued.

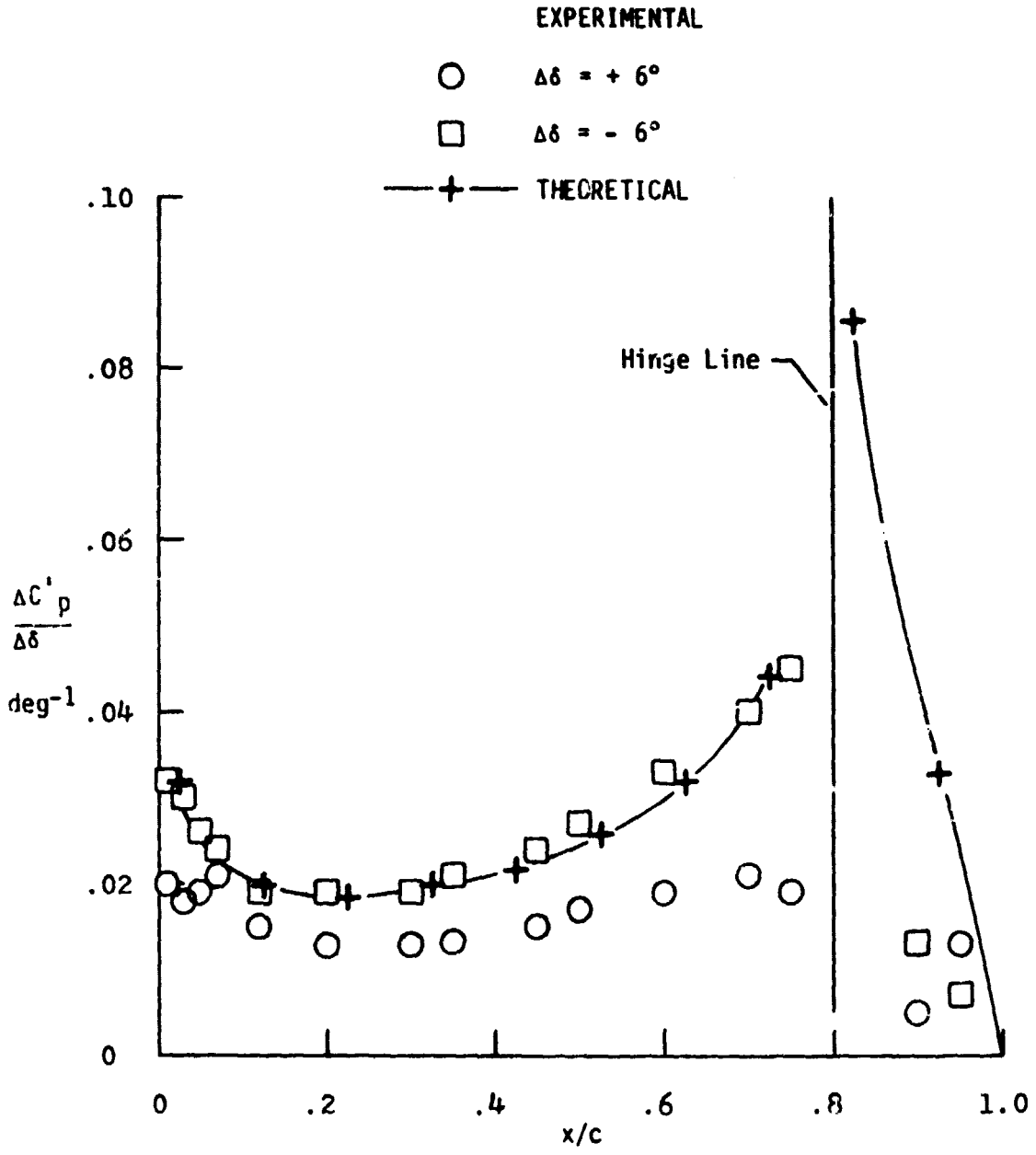

(f) For $\Delta\delta = \pm 6°$ and $\alpha = 2.85°$.

Figure 8.- Concluded.

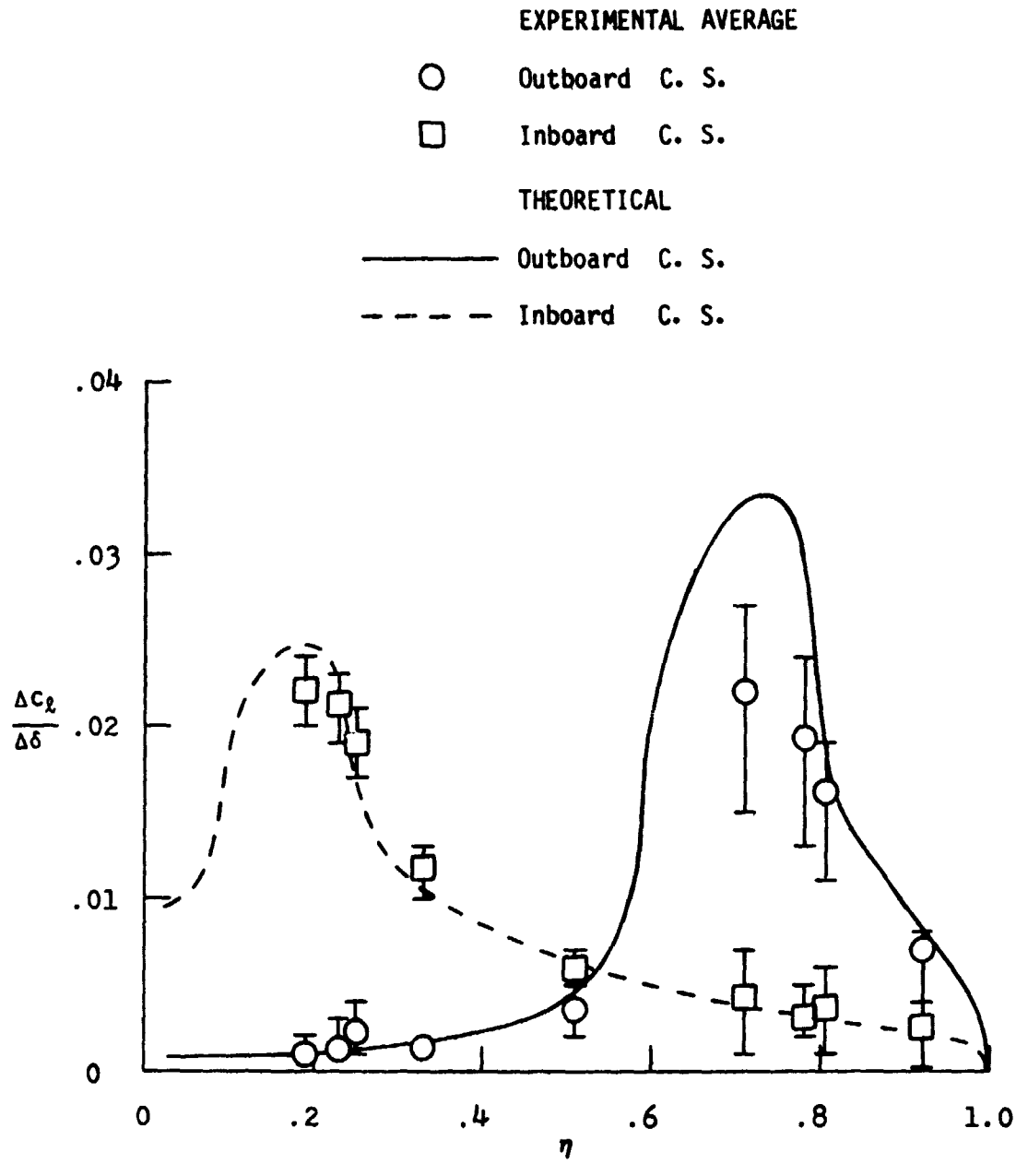

Figure 9. - Spanwise lift distributions for incremental control-surface deflections.

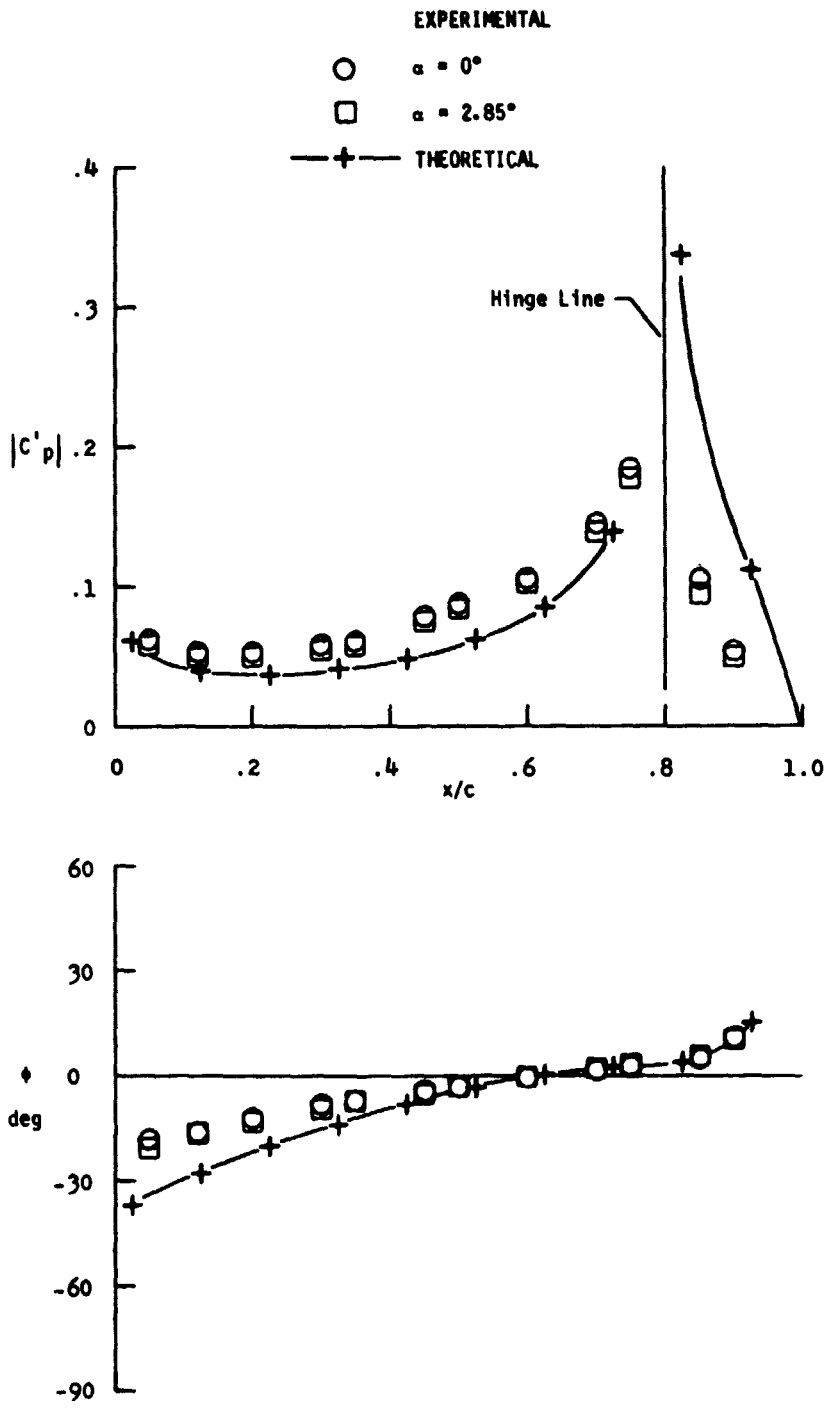

(a) For $\delta = \pm 4°$ and $k = 0.14$ ($f = 5$ Hz).

Figure 10. - Magnitude and phase angle of chordwise lifting-surface unsteady-pressure distribution at semispan station $\eta = 0.18$, due to oscillating inboard control surface.

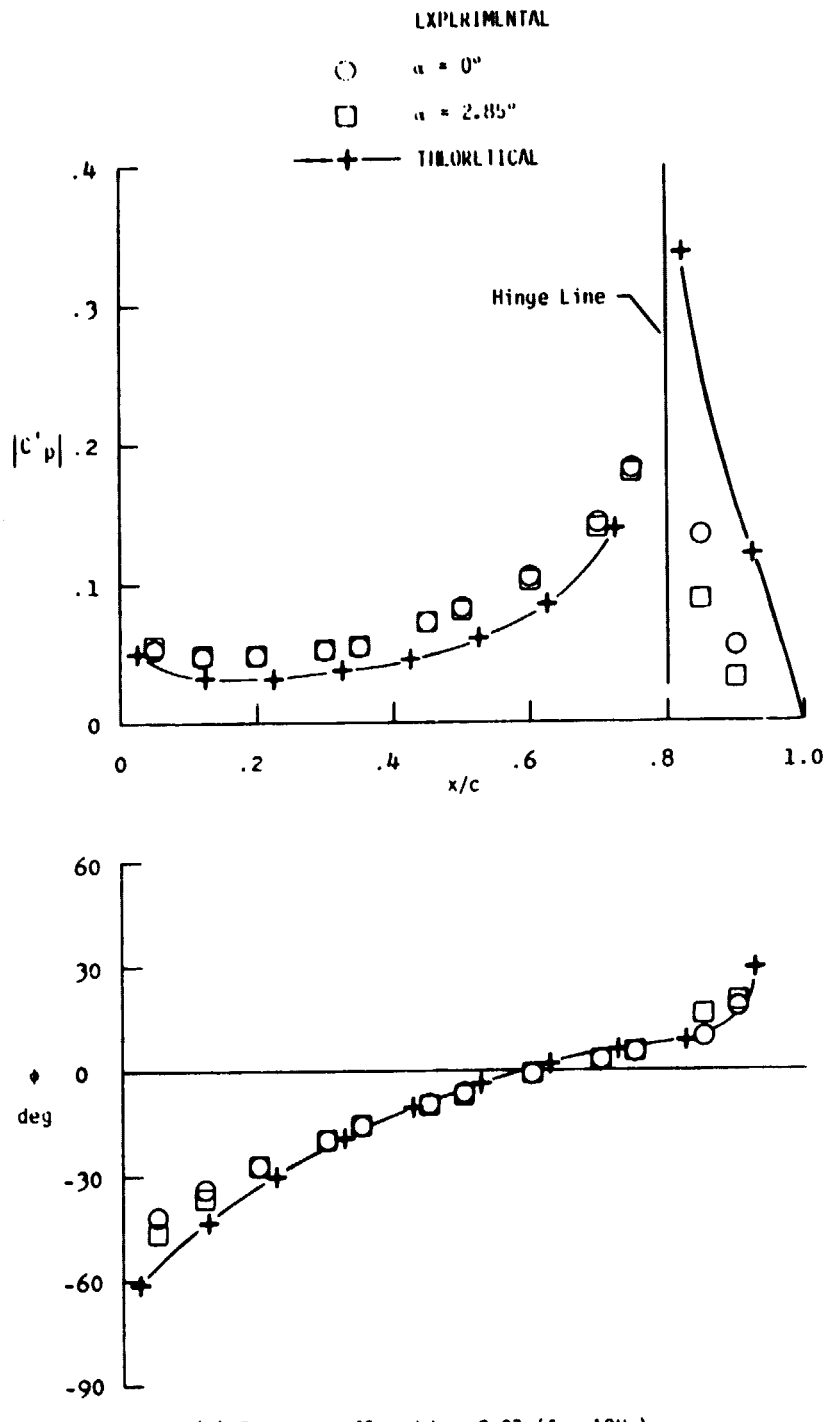

(b) For $\delta = \pm 4°$ and $k = 0.27$ ($f = 10Hz$).

Figure 10.- Continued.

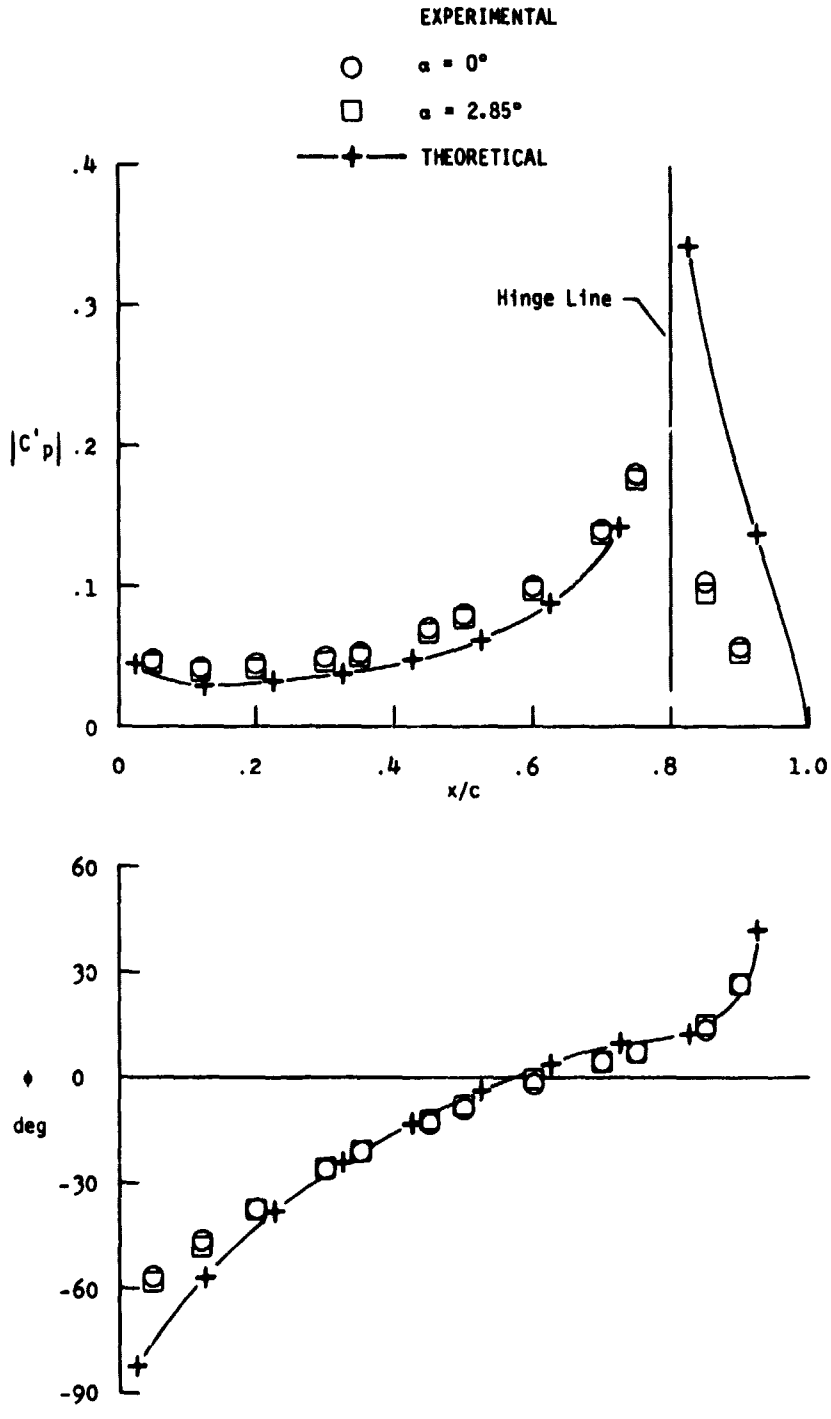

(c) For $\delta = \pm 4°$ and $k = 0.41$ ($f = 15$Hz).

Figure 10.- Concluded.

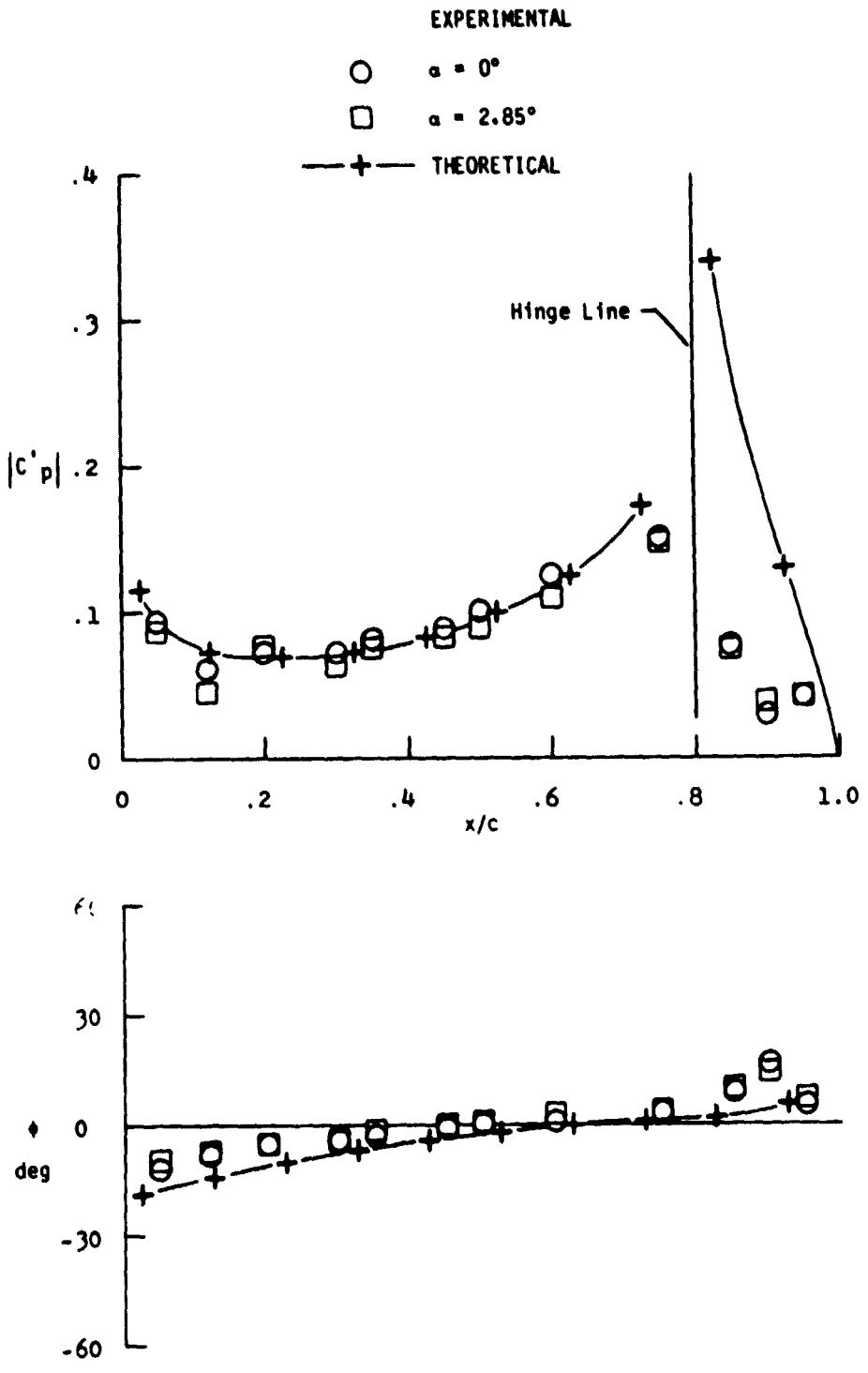

(a) For δ = ± 4° and k = 0.14 (f = 5Hz).

Figure 11. - Magnitude and phase angle of chordwise lifting-surface unsteady-pressure distribution at semispan station η = 0.71, due to oscillating outboard control surface.

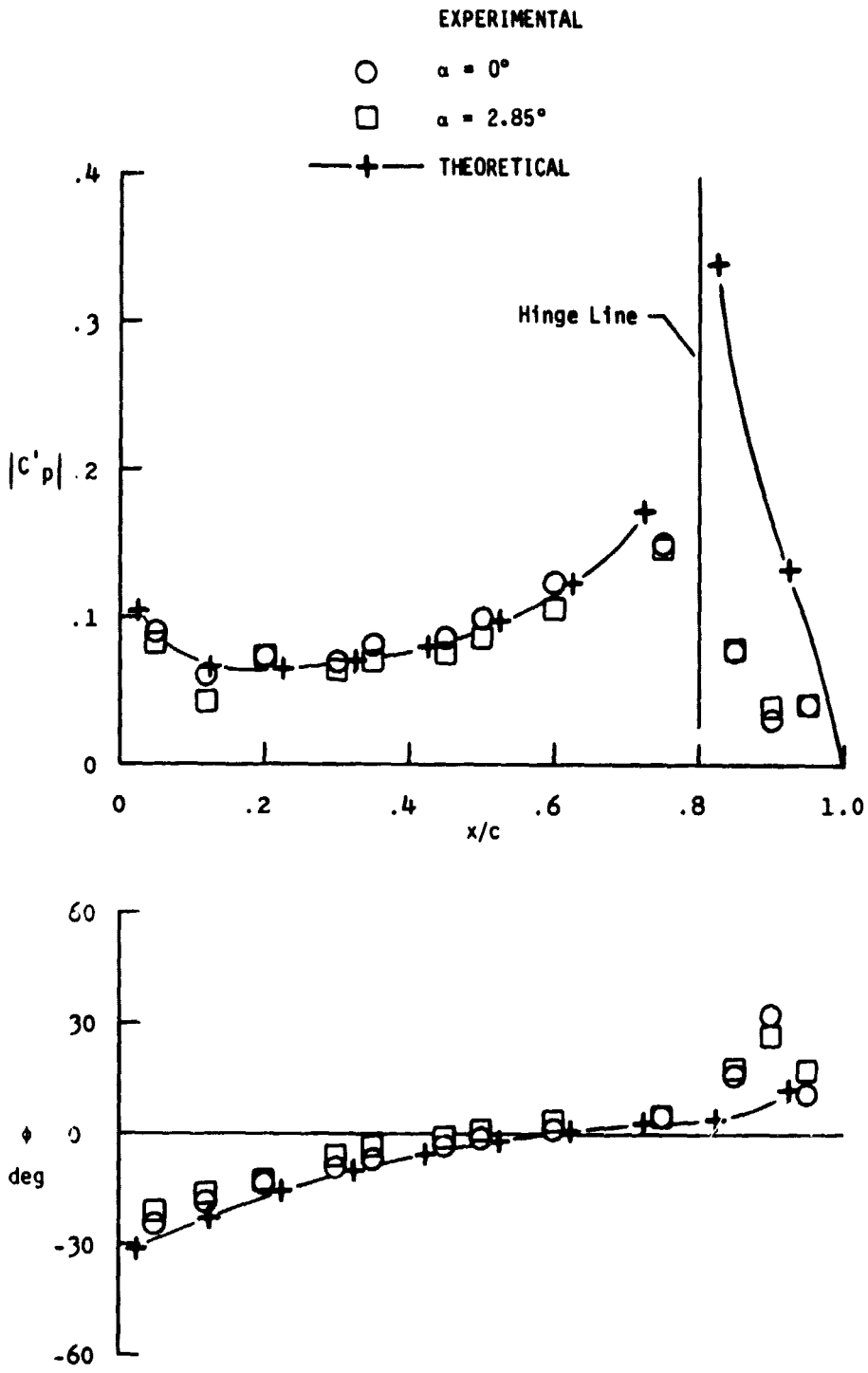

(b) For δ = ± 4° and k = 0.27 (f = 10Hz).

Figure 11.- Continued.

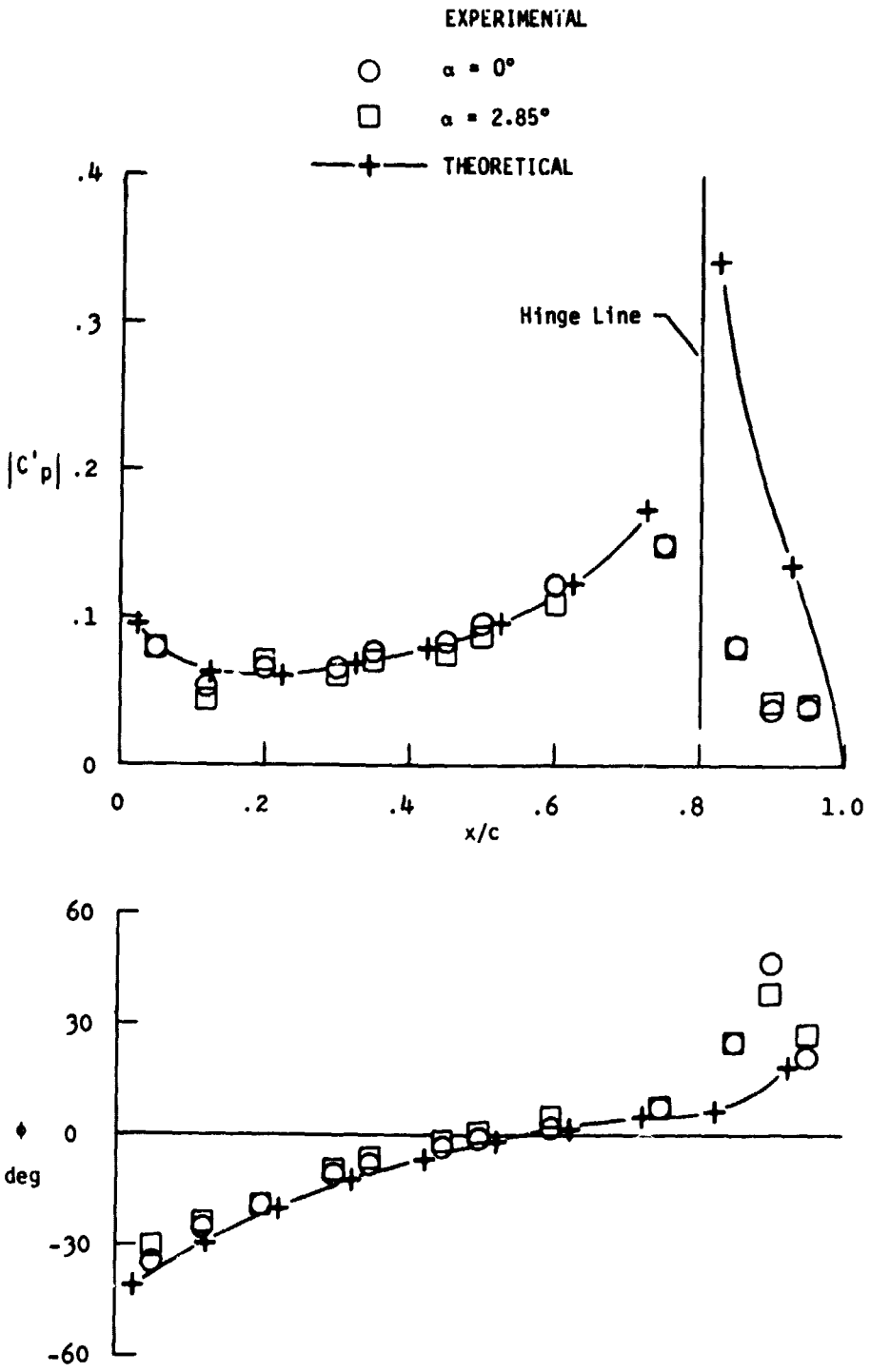

(c) For $\delta = \pm 4°$ and $k = 0.41$ ($f = 15$Hz).

Figure 11.- Concluded.